Middle Eocene greenhouse warming facilitated by diminished weathering feedback

Robin van der Ploeg[1*], David Selby[2,3], Margot J. Cramwinckel[1], Yang Li[4,5], Steven M. Bohaty[6], Jack J. Middelburg[1], Appy Sluijs[1]

[1]Department of Earth Sciences, Faculty of Geosciences, Utrecht University, Utrecht, The Netherlands

[2]Department of Earth Sciences, Durham University, Durham, DH1 3LE, UK

[3]State Key Laboratory of Geological Processes and Mineral Resources, School of Earth Resources, China University of Geosciences, Wuhan, 430074, Hubei, China

[4]Department of Geology and Geophysics, Yale University, New Haven, Connecticut 06511, USA

[5]State Key Laboratory of Lithospheric Evolution, Institute of Geology and Geophysics, Chinese Academy of Sciences, Beijing, 10029, China

[6]Ocean and Earth Science, National Oceanography Centre, University of Southampton Waterfront Campus, Southampton, SO14 3ZH, UK

[*]E-mail: R.vanderPloeg@uu.nl

The Middle Eocene Climatic Optimum (MECO) represents a ~500 kyr period of global warming ~40 million years ago and is associated with a rise in atmospheric CO_2 concentrations, but the cause of this CO_2 rise remains enigmatic. Here we show, based on osmium isotope ratios ($^{187}Os/^{188}Os$) of marine sediments and published records of the carbonate compensation depth (CCD), that the continental silicate weathering response to the inferred CO_2 rise and warming was strongly diminished during the MECO – in contrast to expectations from the silicate weathering thermostat hypothesis. We surmise that global early and middle Eocene warmth gradually diminished the weatherability of continental rocks and hence the strength of the silicate weathering feedback, allowing for the prolonged accumulation of volcanic CO_2 in the oceans and atmosphere during the MECO. These results are supported by carbon cycle modeling simulations, which highlights the fundamental importance of a variable weathering feedback strength in climate and carbon cycle interactions in Earth's history.

The chemical weathering of silicate rocks on the continents represents a negative feedback mechanism that is generally considered to modulate atmospheric CO_2 levels and Earth's climate on geological timescales[1,2]. This phenomenon has been studied for various carbon cycle perturbations and episodes of global warming in the geological past, including Pleistocene deglaciations, the Paleocene-Eocene Thermal Maximum (PETM; ~56 Ma) and the Cretaceous and Jurassic Oceanic Anoxic Events (OAEs), mainly through the application of depositional isotope ratios of marine sediments that are sensitive to shifts in weathering fluxes or compositions on the appropriate timescales[3–5]. For many of these phases, it is now relatively well established that enhanced continental weathering contributed to CO_2 drawdown and climatic recovery[4,6,7]. However, the available data spanning the Middle Eocene Climatic Optimum (MECO; ~40 Ma) pose questions regarding the functioning of the

45 weathering feedback[8]. Over a period of ~500 kyr, global ocean temperatures rose gradually
46 by up to ~5 °C in association with an increase in atmospheric CO_2 concentrations, sourced
47 from a reservoir with a stable carbon isotopic composition ($\delta^{13}C$) similar to that of the ocean[9–
48 13]. Importantly, the inferred rise in atmospheric CO_2 and temperature over ~500 kyr during
49 the MECO should have led to increased weathering and alkalinity supply to the oceans, but
50 reconstructions show that the oceans acidified[8,10]. Therefore, reconstructing the global
51 weathering response during the MECO is instrumental to improving our fundamental
52 understanding of carbon cycle dynamics on such intermediate timescales of ~500 kyr.

53 A promising proxy to reconstruct changes in continental weathering during the MECO
54 is the osmium isotope ratio of marine sediments at the time of deposition ($^{187}Os/^{188}Os_{initial}$, or
55 Os_i)[14,15]. The $^{187}Os/^{188}Os$ ratio of the global ocean is governed by the relative input of
56 radiogenic Os ($^{187}Os/^{188}Os$ = ~1.4) through continental weathering of ancient crustal rocks,
57 and the relative input of unradiogenic Os ($^{187}Os/^{188}Os$ = 0.13) through hydrothermal activity
58 at mid-ocean ridges and weathering of fresh mantle-derived rocks, with additional
59 contributions from extraterrestrial sources[14]. Osmium is a quasi-conservative element that is
60 well-mixed in the ocean and has a short oceanic residence time (generally ~10^4 yr in the open
61 ocean, but values of ~10^3 yr have been inferred for very restricted settings)[14,16]. Variations in
62 the $^{187}Os/^{188}Os$ ratio of seawater are thus indicative of changes in continental weathering
63 relative to the other sources on timescales shorter than, or similar to, climate and carbon cycle
64 processes such as greenhouse warming, ocean acidification and carbonate compensation[14,15].
65 Seawater Os is incorporated in the metalliferous and organic phases of marine sediments
66 without isotopic fractionation, and remains a closed isotopic system from the time of
67 deposition[17–19]. As such, Os_i values are calculated on the basis that radiogenic ^{187}Os ingrowth
68 is derived solely from post-depositional ^{187}Re (rhenium) decay. Shifts to higher (radiogenic)
69 Os_i values, which are attributed to a global increase in continental weathering rates, have been

recorded for carbon cycle perturbations such as the Toarcian OAE and the PETM and Eocene Thermal Maximum 2 (ETM2) transient global warming events[5,15,20].

A second parameter that is often used to constrain changes in continental weathering is the carbonate compensation depth (CCD). The CCD is the depth in the oceans at which carbonate delivery is balanced by carbonate dissolution, and is modulated by the interplay of volcanic CO_2 degassing, the weathering of silicate rocks and organic-rich sediments on land and the burial of marine carbonates and organic carbon[21]. As such, changes in the position of the CCD as reflected in sediments play a crucial role in reconstructions of carbon cycle change, both on multi-million year timescales and during transient perturbations such as the MECO[22].

In this study, we present Os_i records of marine sediments from three locations in different ocean basins in combination with a compilation of published CCD records[8] to reconstruct global changes in continental weathering during the MECO. Rather than an Os_i increase expected from globally enhanced weathering, we document a modest, global Os_i decrease during the MECO that may represent an episode of enhanced volcanism and associated basalt weathering. In fact, prolonged CCD shoaling precludes an increase in total continental weathering rates in response to CO_2 rise and greenhouse warming. We employ a series of simulations with the carbon cycle model LOSCAR[23] together with an independent osmium cycle model to demonstrate that this combination of observations can only be successfully reconciled on MECO timescales by invoking enhanced volcanism together with a diminished continental weathering feedback. Finally, we surmise that such a reduced silicate weathering feedback may have resulted from a progressive decrease in the weatherability of the continents during the Eocene. A variable silicate weathering feedback strength may have been of importance for other enigmatic climate and carbon cycle perturbations in Earth's history.

95

Results

Middle Eocene osmium isotope records

We present the Re-Os data and Os_i values for middle Eocene sediments from Ocean Drilling Program (ODP) Site 959 in the equatorial Atlantic along the African continental margin, ODP Site 1263 on the Walvis Ridge in the South Atlantic, and Integrated Ocean Drilling Program (IODP) Site U1333 in the equatorial Pacific (Fig. 1; Supplementary Data 1; Supplementary Fig. 1 – 3). The Re and Os abundances are significantly enriched in the relatively organic-rich, siliceous sediments of Site 959 (Re = 10 – 60 ppb, Os = 100 – 300 ppt) relative to the carbonate-rich pelagic sediments of Sites 1263 and U1333 (Re = 0.02 – 0.2 ppb, Os = 10 – 40 ppt). The abundances of ^{192}Os, the Os isotope best representing the amount of hydrogenous Os chelated by organic matter at the time of deposition[24], increase slightly over the study interval at Site 959, but are essentially stable at the other two sites (Fig. 1). We calculate Os_i values of 0.46 to 0.60 at all study sites (Fig. 1), which is in good agreement with previously published middle Eocene Os_i values from Site 959 sediments[25,26] and with Os_i values from ferromanganese crusts that document a progressive increase in the $^{187}Os/^{188}Os$ composition of seawater during the Cenozoic[27–29] (Fig. 2).

At Site 959, the Os_i values range between approximately 0.56 – 0.60 for most of the middle Eocene study interval, with the exception of a decrease to 0.51 during the MECO at ~580 mbsf (Fig. 1). Importantly, the lack of an increase in the Os_i values during the MECO implies that weathering rates of felsic silicate rocks did not increase in response to CO_2 rise and accompanied warming, while such an increase would be expected from theory and the Os_i records from the abovementioned analogous carbon cycle perturbations[3,7,15] (Fig. 2b). Furthermore, the relative invariability of both the Os_i records and the ^{192}Os abundances –

120 which scale to organic matter content – implies that the balance of Os fluxes to the oceans and
121 uptake of Os in sedimentary organic matter did not appreciably change during the MECO.

122 Although the magnitude of the negative Os_i shift at Site 959 is small (~0.05), it
123 exceeds the maximum analytical uncertainty ($2\sigma = 0.01$) by a factor of 5. The shift starts at
124 the onset of MECO warming and is also present at Sites 1263 and U1333, where it is similar
125 in magnitude (Fig. 1 and 2). Interestingly, the Os_i profile of Site U1333 is characterized by
126 two separate excursions to lower, less radiogenic values rather than the gradual and
127 continuous decrease that is observed at Site 959. The Os_i profile at Site 1263 shows
128 intermediate trends. Nevertheless, the lowest Os_i values in all three records occur towards the
129 end of the MECO, which is coincident with the peak warming phase[10]. In addition, the return
130 towards pre-MECO values is synchronous with the termination of the MECO at all three sites,
131 implying that the Os_i shift lasted for the entire duration of the event (~500 kyr). The absolute
132 Os_i values differ slightly between sites, likely because of differences in coastal proximity and
133 oceanographic setting[30,31]. However, the general timing and magnitude of the Os_i shift are
134 reproduced at all sites, indicating that it records a change in the $^{187}Os/^{188}Os$ composition of
135 the global ocean. The global character and synchroneity of the Os_i shift at the end of the
136 MECO indicate that osmium isotope stratigraphy is a promising tool to correlate the event
137 between sites in future studies (Fig. 2a).

138 In principle, the modest negative Os_i shift may be caused by an increase in the
139 unradiogenic Os flux from hydrothermal and/or extraterrestrial sources, a decrease in the
140 radiogenic Os flux from continental weathering, or a decrease in the $^{187}Os/^{188}Os$ composition
141 of the continental weathering flux through a transient change in the exposure of different rock
142 types such as basalts to weathering[7]. There is no evidence for an extraterrestrial impact during
143 the MECO. Furthermore, a reduction in continental silicate weathering rates during an
144 episode of greenhouse warming seems paradoxical and unlikely, even though our Os_i records

clearly show no evidence of the expected increase in continental weathering. It is difficult to exclude a warming-induced change in regional climates and precipitation patterns – which could have affected the contributions of rock types with different $^{187}Os/^{188}Os$ compositions to the continental weathering flux[3,32] – as a cause for the Os_i shift. However, this would still require a different cause for MECO warming.

Finally, the Os_i shift could reflect a short-lived increase in mid-ocean ridge hydrothermal activity or an episode of increased volcanism and associated weathering of mafic silicate rocks[24,33,34]. Mass balance calculations with a progressive two-component mixing model that involves seawater and basalts (see Methods; Supplementary Data 2) show that the Os_i shift across the MECO may correspond to a 10 – 15 % increase in the contribution of the mantle-derived Os flux relative to the continental Os flux. Although there is no indication for the emplacement of a large igneous province during the middle Eocene[8], an episode of volcanic activity at mid-ocean ridges or on land could have increased the Os flux from basalts and consequently resulted in a decrease of the $^{187}Os/^{188}Os$ composition of the oceans that is consistent with our Os_i records. Moreover, enhanced volcanism would provide a mechanism for the atmospheric CO_2 rise that has been inferred for the MECO[8,11], perhaps similar to the Late Cretaceous episode of greenhouse warming associated with volcanic eruptions from the Deccan Traps[33,35,36]. Potential events that have been dated at approximately the right age in the middle Eocene include (1) a pulse of metamorphic decarbonation associated with Himalayan uplift and metamorphism[37,38], (2) increased arc volcanism around the Pacific rim[39] and especially in the Caribbean, related to an ignimbrite flare-up in the Sierra Madre Occidental of Mexico[40–42], (3) an episode of magmatism in the East African Rift zone[43], in particular in Southern Ethiopia and Northern Kenya[44,45], and/or (4) mid-ocean ridge volcanism in the North Atlantic, due to rifting in East Greenland and activity of the Iceland hotspot[46–48]. However, the timing and magnitude of these volcanic

events are at present not sufficiently well resolved to establish a direct causal link with the MECO. Additionally, it is unclear if increased Himalayan uplift and metamorphism would be compatible with the observed negative Os_i shift, as the Himalayas are generally considered to contribute relatively radiogenic Os to the continental weathering flux[49,50]. Yet, the effects of Himalayan uplift and subsequent weathering on the Cenozoic Os_i record are likely small[51,52].

Carbon and osmium cycle modeling

Enhanced volcanism and/or hydrothermal activity may represent the most parsimonious scenario to explain the modest negative Os_i shift and atmospheric CO_2 rise during the MECO. However, a strong silicate weathering response to greenhouse warming through focused weathering of fresh basalts is in disagreement with the extensive carbonate dissolution observed in deep ocean basins[8,10]. Therefore, total continental weathering fluxes must have remained approximately constant during the event. Collectively, the available data indicate that CO_2 was added to the ocean-atmosphere system through enhanced volcanism, leading to warming, but was not neutralized through the silicate weathering feedback, leading to sustained ocean acidification.

To test the plausibility of scenarios involving enhanced volcanism and/or diminished continental weathering during the MECO, we performed a series of carbon cycle simulations with the box model LOSCAR[23] by prescribing fluxes with the transient shift that is inferred from our Os_i records (see Methods; Fig. 3; Supplementary Fig. 4 – 9). For consistency, we have also modeled the $^{187}Os/^{188}Os$ composition of the global ocean by applying the same LOSCAR carbon cycle fluxes as forcing to a box model of the Os cycle (see Methods; Supplementary Software). In addition to a ~0.05 decrease in the $^{187}Os/^{188}Os$ ratio of seawater, our target scenario for the MECO involves a rise in atmospheric CO_2 concentrations, a slight increase in the $\delta^{13}C$ of dissolved inorganic carbon (DIC) in the deep ocean and a shoaling of

195 the carbonate compensation depth (CCD) over ~500 kyr[8]. Since there are no high-resolution
196 pCO_2 records available for the MECO, the target scenario includes an approximate doubling
197 of atmospheric CO_2 concentrations relative to middle Eocene background values of 500 –
198 1000 ppmv[11,53]. Furthermore, the magnitude of CCD change during the event possibly varied
199 between the different ocean basins[10], so we incorporate a conservative estimate of at least 500
200 m shoaling in the Atlantic and Pacific in our target scenario.

201 All model simulations result in a decrease in the $^{187}Os/^{188}Os$ ratio of seawater (Fig. 3;
202 Supplementary Fig. 4 – 9). Although a gradual, linear increase in volcanism of 10 – 20 %
203 over ~500 kyr is sufficient to cause CO_2 accumulation in the ocean-atmosphere system and
204 hence global warming on MECO timescales, this scenario results in a deepening of the CCD
205 instead of the observed shoaling (Fig. 3; Supplementary Fig. 4)[8,10]. A similar behavior of the
206 CCD is observed in previous LOSCAR simulations of the MECO[8] and the Late Cretaceous
207 warming episode[36]. Crucially, the model is only able to reproduce CO_2 rise in conjunction
208 with shoaling of the CCD on these timescales if we invoke enhanced volcanism together with
209 a diminished weathering feedback by maintaining the silicate and carbonate weathering fluxes
210 constant (Fig. 3; Supplementary Fig. 5). Although the magnitude of this modeled CCD
211 response is smaller than the shoaling inferred from deep-sea carbonate records[8,10], we note
212 that the model may underestimate CCD changes because it does not account for the additional
213 effects of biological carbonate compensation[54]. Such a reduction in net carbonate production
214 resulting from ocean acidification might amplify the CCD response for a given CO_2 rise. In
215 all scenarios, the model reproduces the modest increase in deep-sea benthic foraminifer stable
216 carbon isotope ratios ($\delta^{13}C$) during the event[9,10], because of a resulting decrease in carbonate
217 versus constant organic carbon burial. Finally, the relatively rapid termination of the MECO
218 is forced by a recovery of silicate weathering. We note that this does not need to represent a
219 pronounced tectonic event, as the absolute magnitude of the flux imbalances is relatively

small, but regionally enhanced weathering in the aftermath of the MECO would be consistent with observations from the Tethys region[55].

Discussion

To reconcile our Os_i records and model results with global warming and atmospheric CO_2 rise on MECO timescales[8–11], we hypothesize that a long-term reduction in the strength of the negative silicate weathering feedback occurred in the Eocene[56,57], due to a progressive reduction in the weatherability of the continents – the sum of all factors affecting chemical weathering other than climate[58,59]. For millions of years prior to the MECO, the Earth was generally characterized by high atmospheric CO_2 levels[53] and very warm climates[60] (Supplementary Fig. 10), as well as flat continental relief. Thick, cation-depleted soils developed and transport-limited weathering regimes prevailed[61,62], and consequently the weatherability of Earth's surface may have gradually decreased over the course of the Eocene. Indeed, such a progressive reduction in weathering feedback strength during the Eocene has been inferred from inverse modeling simulations of weathering fluxes based on Cenozoic pCO_2 and $\delta^{13}C$ records[57] (Fig. 2c). With the strength of the weathering feedback strongly diminished, a small increase in volcanism or hydrothermal activity would lead to the accumulation of large amounts of CO_2 in the ocean-atmosphere system, resulting in prolonged warming and ocean acidification during the MECO.

Changes in weatherability have also been suggested to explain other episodes of apparent decoupling between silicate weathering and climate[59], for example during major glaciations in the Paleozoic and Neoproterozoic[63–65]. Our interpretations of a limited weathering response during the MECO suggest that a variable silicate weathering feedback strength[57] can indeed act as a driver for sustained global warming on geological timescales, with potential importance to other enigmatic phases of carbon cycle change in Earth's history.

245 Moreover, a variable feedback strength governed by the interplay between tectonics, climate
246 and the weatherability of the continents fundamentally challenges the parameterization of the
247 silicate weathering feedback in carbon cycle models, especially those used to model transient
248 perturbations such as the OAEs and the PETM. We therefore argue that future studies of these
249 events should focus on exploring changes in temperature, atmospheric CO_2 and the CCD in
250 conjunction with the strength of the weathering feedback.
251

Methods

Sampling

The samples used in this study were derived from middle Eocene sedimentary units from three different sites: organic-rich sediments from ODP Site 959 in the equatorial Atlantic along the African continental margin, carbonate-rich pelagic sediments from ODP Site 1263 on the Walvis Ridge in the south Atlantic and carbonate-rich pelagic sediments from IODP Site U1333 in the equatorial Pacific (Supplementary Fig. 1). The total organic carbon (TOC) abundances of these middle Eocene sediments range between 0.1 and 2 %, with the highest TOC abundances occurring at Site 959[66]. Rock samples of 20 – 40 g were selected across the middle Eocene interval between approximately 42 and 38 Ma, with the highest sampling resolution across the MECO.

Analyses

Bulk samples were freeze-dried or oven-dried at 50 °C and subsequently powdered using a ceramic pestle and mortar, in order to homogenize the Re and Os within the samples. Contact with metal surfaces was avoided so as not to contaminate the sample set. All Re and Os isotope analyses were performed at the Laboratory for Source Rock and Sulfide Geochronology and Geochemistry, and the Arthur Holmes Laboratory at the Durham Geochemistry Centre, Durham University (UK). Samples were digested in a CrO_3-H_2SO_4 solution (0.25 g/g CrO_3 in 8 mL of 4N H_2SO_4) following the well-established methods of Selby & Creaser (2003)[67], which have been shown to significantly limit the contribution of detrital Re and Os to the hydrogenous fraction bound to organic matter.

Powdered samples of approximately 0.3 – 1 g were loaded into Carius tubes with a known amount of ^{185}Re + ^{190}Os tracer solution (spike) and dissolved in 8 mL of CrO_3-H_2SO_4

277 solution. The Carius tubes were then sealed and heated in an oven at 220 °C for 48 hours.
278 Osmium was isolated from the CrO_3-H_2SO_4 sample solution by using solvent extraction with
279 chloroform ($CHCl_3$) and then back extracted by hydrobromic acid (HBr). The Os was further
280 purified through micro distillation. Rhenium was isolated by evaporating 1 mL of the CrO_3-
281 H_2SO_4 sample solution to dryness, followed by solvent extraction involving sodium
282 hydroxide (NaOH) and acetone (C_3H_6O)[68,69]. The Re was further purified by anion
283 chromatography.

284 Following purification, the Re and Os fractions were loaded onto Ni and Pt filaments,
285 respectively, together with 0.5 µL $BaNO_3$ and BaOH activator solutions, respectively[67].
286 Rhenium and osmium isotope ratios were determined by negative thermal ionization mass
287 spectrometry (N-TIMS), using Faraday cups for Re and a Secondary Electron Multiplier
288 (SEM) for Os in peak-hopping mode.

289 Re and Os isotope ratios were corrected for instrumental mass fractionation, as well as
290 spike and blank contributions. Procedural blanks for Re and Os in this study were 12 ± 3 pg/g
291 and 0.07 ± 0.05 fg/g, respectively, with an $^{187}Os/^{188}Os$ value of 0.25 ± 0.15 (n = 3). The
292 $^{187}Re/^{188}Os$ and $^{187}Os/^{188}Os$ uncertainties (2σ) include full propagation of uncertainties in
293 weighing, mass spectrometer measurements, spike calibrations, blank corrections and
294 reproducibility of standards.

295 The $^{187}Os/^{188}Os_{initial}$ ratios (Os_i) were calculated by correcting for post-depositional
296 ^{187}Re decay over time with the following equation:

297

298 $$^{187}Os/^{188}Os_{\text{initial}}\,(Os_{\text{i}}) = {}^{187}Os/^{188}Os_{\text{measured}} - {}^{187}Re/^{188}Os_{\text{measured}} * \left(e^{\lambda t} - 1\right) \quad (1)$$

299

300 where λ is the ^{187}Re decay constant ($1.666 * 10^{-11}$ yr^{-1})[70] and t is the age of the rock. Given the
301 high Re abundances in the organic-rich sediments from Site 959, we have used best estimates

for the depositional ages of each of these samples. An age of 40 Ma was used for all samples from Sites 1263 and U1333, because improved age estimates would result in variations in Os_i values of 0.1 % or less on average. All results are listed in Supplementary Data 1. The Re-Os isotopic system is expected to have remained closed for the sample set, given that the cores were all fresh, unweathered, and showed no evidence of post-depositional events (e.g., veining, etc.). Further, where the Re-Os data has sufficient spread in isochron plot space to yield statistically robust isochrons, a geologically reasonable Re-Os isochron age is obtained (e.g., Site 959; see below for details).

Evaluation of Re and Os data

Although the studied samples were collected for evaluating changes in Os_i rather than establishing isochrons, the Re-Os data of the sediments from Site 959 show a positive correlation between $^{187}Re/^{187}Os$ and $^{187}Os/^{188}Os$, which results in an isochron age that is in good agreement with the age of the MECO between 40.5 and 40.0 Ma (Supplementary Fig. 2 and 3). In contrast, the $^{187}Re/^{187}Os$ and $^{187}Os/^{188}Os$ data for Sites 1263 and U1333 do not have sufficient spread in isochron plot space, and hence cannot yield statistically geologically meaningful age estimates.

Age models

We adopt the age model of Cramwinckel et al. (in press)[13] for Site 959 (Supplementary Fig. 11). This is based on initial[71] and recently improved[13] calcareous nannofossil biostratigraphy. The model also uses the long-term $^{187}Os/^{188}Os$ minimum at 34.65 Ma recorded at this site[26], and TEX_{86} data that mark the MECO warming[13]. Moreover, we use the highest TEX_{86} value during the MECO peak warming and the lowest TEX_{86} value at the onset of the MECO as reported by Cramwinckel et al. (in press)[13] to tentatively correlate to minima and maxima in

the $\delta^{18}O$ records of Bohaty et al. (2009)[10], which were assigned ages of 40.06 and 40.52 Ma, respectively. Better age models are available for the other two sites. For Site 1263, we use a published age model[10] based on magnetostratigraphy and bulk carbonate $\delta^{18}O$ and $\delta^{13}C$ chemostratigraphy. For Site U1333, an astronomically calibrated magnetostratigraphic age model[72] was used in combination with calcareous nannofossil events[73]. All ages were adjusted to the framework of the GTS 2012[74] and tie points for the age models are listed in Supplementary Tables 1, 2 and 3.

Calculating changes in Os fluxes across the MECO

The $^{187}Os/^{188}Os$ composition of seawater is controlled by the balance between input fluxes from continental, mantle-derived and extraterrestrial sources. However, the flux of extraterrestrial Os is generally assumed to be negligible and constant[75,76], so our Os_i records can be used to directly infer changes in relative contributions of the continental and mantle-derived Os sources across the MECO. To evaluate an increase in the mantle-derived Os flux, we developed a progressive, two-component mixing model for the release of Os from mantle-derived basalts that incorporates both the Os abundance and $^{187}Os/^{188}Os$ composition of seawater and basalts. This model is an adaptation of the two-component mixing model for strontium (Sr) isotopes of Faure (1986, Equations (9.2) and (9.10))[77], with modifications to consider the larger range of Os isotope variations in comparison to Sr isotope variations.

From the relative molar concentrations of natural Os isotopes, we know:

$$\frac{[Os]-[^{187}Os]}{[^{188}Os]} = 7.4 \quad (2)$$

where [*Os*] represents the molar concentration (in mol / kg) of total Os (i.e., ^{186}Os + ^{187}Os + ^{188}Os + ^{189}Os + ^{190}Os + ^{192}Os), and [^{187}*Os*] and [^{188}*Os*] represent the molar concentrations (in mol / kg) of ^{187}Os and ^{188}Os, respectively[78].

Equation (2) can be rewritten as:

$$[^{187}Os] = \frac{R}{7.4+R}[Os] \quad (3)$$

$$[^{188}Os] = \frac{1}{7.4+R}[Os] \quad (4)$$

where $R = [^{187}Os]/[^{188}Os]$.

Two-component mixing between seawater and basalts can then be expressed for both ^{187}*Os* and ^{188}*Os* as:

$$[^{187}Os]_{\mathrm{mix}} = \frac{[^{187}Os]_{\mathrm{sw}} * M_{\mathrm{sw}} + [^{187}Os]_{\mathrm{bas}} * M_{\mathrm{bas}}}{M_{\mathrm{sw}} + M_{\mathrm{bas}}} \quad (5)$$

$$[^{188}Os]_{\mathrm{mix}} = \frac{[^{188}Os]_{\mathrm{sw}} * M_{\mathrm{sw}} + [^{188}Os]_{\mathrm{bas}} * M_{\mathrm{bas}}}{M_{\mathrm{sw}} + M_{\mathrm{bas}}} \quad (6)$$

where *M* represents the mass of a component (in kg) and the subscripts *sw*, *bas* and *mix* represent seawater, basalts and the eventual mix between the two, respectively.

We now define:

$$\Delta M_{\mathrm{bas}} = \frac{M_{\mathrm{bas}}}{M_{\mathrm{sw,initial}}} \quad (7)$$

$$f = \frac{\Delta M_{\mathrm{bas}}}{M_{\mathrm{sw,progressive}} + \Delta M_{\mathrm{bas}}} = \frac{\Delta M_{\mathrm{bas}}}{M_{\mathrm{mix}}} \quad (8)$$

where ΔM_{bas} is an infinitesimal representing the mass of basalts added during a mixing step relative to the mass of seawater initially present, and f represents the amount of basalts added during a mixing step relative to the total amount of seawater and basalts present during progressive mixing (M_{mix}).

Equations (3) – (8) can then be combined as follows:

$$[^{187}Os]_{\mathrm{mix}} = f * [^{187}Os]_{\mathrm{bas}} + (1-f) * [^{187}Os]_{\mathrm{sw}}$$

$$= f * \frac{R_{\mathrm{bas}}}{7.4+R_{\mathrm{bas}}}[Os]_{\mathrm{bas}} + (1-f) * \frac{R_{\mathrm{sw}}}{7.4+R_{\mathrm{sw}}}[Os]_{\mathrm{sw}} \quad (9)$$

$$[^{188}Os]_{\mathrm{mix}} = f * [^{188}Os]_{\mathrm{bas}} + (1-f) * [^{188}Os]_{\mathrm{sw}}$$

$$= f * \frac{1}{7.4+R_{\mathrm{bas}}}[Os]_{\mathrm{bas}} + (1-f) * \frac{1}{7.4+R_{\mathrm{sw}}}[Os]_{\mathrm{sw}} \quad (10)$$

Finally, dividing equation (9) by equation (10) yields:

$$R_{\mathrm{mix}} = \frac{[^{187}Os]_{\mathrm{mix}}}{[^{188}Os]_{\mathrm{mix}}} = \frac{f*\frac{R_{\mathrm{bas}}}{7.4+R_{\mathrm{bas}}}[Os]_{\mathrm{bas}} + (1-f)*\frac{R_{\mathrm{sw}}}{7.4+R_{\mathrm{sw}}}[Os]_{\mathrm{sw}}}{f*\frac{1}{7.4+R_{\mathrm{bas}}}[Os]_{\mathrm{bas}} + (1-f)*\frac{1}{7.4+R_{\mathrm{sw}}}[Os]_{\mathrm{sw}}} \quad (11)$$

where R is the $^{187}Os/^{188}Os$ composition of the corresponding components (i.e., seawater, basalts and the eventual mix between the two).

Equations (7) – (11) can then be used to estimate the extent of mixing between seawater and basalts during the MECO by progressively calculating R_{mix} until our observed Os_i shift is reproduced (see Supplementary Data 2). We assumed the pre-MECO $^{187}Os/^{188}Os$

ratio of seawater to be ~0.55 based on an average of pre-MECO Os_i values recorded for the three sites and the Os concentration of seawater to be 10 ppq (~53 fmol / kg, similar to present-day values)[14]. Furthermore, we used an $^{187}Os/^{188}Os$ ratio of 0.13 for the mantle and mantle-derived basalts[79,80], as well as an Os abundance of 1 ppt (~5.3 pmol / kg) for basalts[80]. Finally, we assumed that the maximum amount of basalt that can theoretically be added to seawater represents ~1 % of the total mass of the ocean, as estimated for OAE2[31,81], and used increments of 0.01 % for the value of ΔM_{bas}.

Based on an Os_i shift of 0.05 from the pre-MECO value of ~0.55 to a peak MECO value of ~0.50, we calculated a relative increase in the mantle-derived Os flux of ~13 % across the event, which would equal the addition of Os from basalts with a mass of ~0.13 % relative to the total mass of the ocean (Supplementary Data 2). Similar results are obtained if we estimate the relative increase in the ^{188}Os flux, rather than the total Os flux. It is important to note that mantle-derived Os could also have been released to seawater through direct addition from magmatic degassing or hydrothermal inputs instead of basalt dissolution, but regardless of the mechanism, a ~13 % increase in the mantle-derived Os flux during the MECO would be sufficient to reproduce our observed Os_i shift and would correspond to the cumulative release of $\sim 9.4 \cdot 10^6$ mol of mantle-derived Os. We also performed our calculations with the Os_i values of each individual site: for Site 959, an Os_i shift from 0.560 to 0.505 would yield a relative increase in the mantle-derived Os flux of ~14 %; for Site 1263, an Os_i shift from 0.530 to 0.485 would yield an increase of ~12 %; for Site U1333, an Os_i shift from 0.515 to 0.460 would yield an increase of ~16 %. These differences are most likely to be attributed to the resolution of our records. To accommodate for this range of flux estimates, we adopted a best estimate of 10 – 15 % for the increase in the mantle-derived Os flux during the MECO, but also explored the effects of an increase of up to 20 % because we

418 are unlikely to have sampled the lowest Os_i values in any of our records due to the relatively
419 low resolution of our dataset.
420
421 LOSCAR and Os cycle modeling
422 Carbon cycle simulations were performed using the Long-term Ocean-atmosphere-Sediment
423 CArbon cycle Reservoir (LOSCAR) model[23]. In this box model, modified from Walker and
424 Kasting (1992)[82], carbon and several other biogeochemical tracers (e.g. alkalinity, phosphate,
425 oxygen) are cycled through atmospheric and oceanic reservoirs. The model ocean is coupled
426 to a sediment module and consists of surface-, intermediate- and deep-water boxes of the four
427 main Paleogene ocean basins (Atlantic, Indian, Pacific and Tethys). The model is designed to
428 simulate the Paleocene-Eocene Thermal Maximum (PETM) at 56 Ma, but the minor changes
429 in paleogeography compared to the middle Eocene at 40 Ma are not of relevance to the simple
430 LOSCAR model. In these simulations, we use default parameter settings for the Paleogene
431 setup. Equilibrium pCO_2 is set at 750 ppm, consistent with pCO_2 estimates based on planktic
432 foraminifer boron isotope ratios ($\delta^{11}B$)[53], and by default, silicate and carbonate weathering are
433 implemented in the model as a feedback response to atmospheric CO_2 concentrations. The
434 CCD definition follows the default LOSCAR setup and is taken as the sediment depth level at
435 which sedimentary $CaCO_3$ contents fall below 10 wt %.
436 We explored the effects of changes in volcanism and/or continental weathering with
437 the constraints from our Os_i records to assess which scenario is able to reproduce a more
438 realistic MECO target. We first simulated several scenarios with a gradual, linear increase in
439 the volcanic CO_2 flux (+10%, +15% and +20%) over ~500 kyr, either while allowing the
440 silicate and carbonate weathering fluxes to vary in response to CO_2 forcing (Supplementary
441 Fig. 4) or while maintaining these weathering fluxes at constant values (Supplementary Fig.
442 5). Subsequently, we performed several simulations invoking silicate weathering as a forcing

rather than a feedback, by prescribing a gradual, linear decrease in the silicate weathering flux (-10%, -15% and -20%) over ~500 kyr, while keeping the volcanic CO_2 flux and the carbonate weathering flux at constant values (Supplementary Fig. 6). Finally, we tested the effect of an increase in volcanism (+5%) combined with a decrease in silicate weathering (-5%) (Supplementary Fig. 7); the effect of a combined decrease in silicate and carbonate weathering (both -10%) (Supplementary Fig. 8); and the effect of a decrease in silicate weathering (-10%) while maintaining a carbonate weathering feedback (Supplementary Fig. 9). For an overview of all model scenarios, see Supplementary Table 4.

In order to demonstrate that our LOSCAR model simulations are consistent with the Os_i records, the scenarios outlined above were also applied to a separate box model of the Os cycle. This Os cycle model is inspired by the work of Richter & Turekian (1993)[83] and many subsequent studies, including Peucker-Ehrenbrink & Ravizza (2000)[14]. We fully derive the equations used to model the Os cycle in the ocean below.

We first define N as the total molar inventory of Os (including all Os isotopes) in seawater, and ^{187}N and ^{188}N as the molar inventories of ^{187}Os and ^{188}Os in seawater, respectively. The $^{187}Os/^{188}Os$ composition of seawater (R_{sw}) is thus expressed as:

$$R_{\mathrm{sw}} = \frac{^{187}N}{^{188}N} \quad (12)$$

Subsequently, changes in R_{sw} over time can be written as:

$$\frac{dR_{\mathrm{sw}}}{dt} = \frac{d}{dt}\left(\frac{^{187}N}{^{188}N}\right) = \frac{^{188}N\frac{d^{187}N}{dt} - ^{187}N\frac{d^{188}N}{dt}}{(^{188}N)^2} = \frac{1}{^{188}N}\left[\frac{d^{187}N}{dt} - R_{\mathrm{sw}}\frac{d^{188}N}{dt}\right] \quad (13)$$

Multiplying equation (13) by ^{188}N gives:

$$^{188}N\,\frac{dR_{sw}}{dt} = \frac{d^{187}N}{dt} - R_{sw}\,\frac{d^{188}N}{dt} \quad (14)$$

Changes in N, ^{187}N and ^{188}N over time can then be written as follows:

$$\frac{dN}{dt} = F_{riv} + F_{hyd} + F_{ext} - F_{sed} \quad (15)$$

$$\frac{d^{187}N}{dt} = F_{riv}\left(\frac{[^{187}Os]}{[Os]}\right)_{riv} + F_{hyd}\left(\frac{[^{187}Os]}{[Os]}\right)_{hyd} + F_{ext}\left(\frac{[^{187}Os]}{[Os]}\right)_{ext} - F_{sed}\left(\frac{[^{187}Os]}{[Os]}\right)_{sed} \quad (16)$$

$$\frac{d^{188}N}{dt} = F_{riv}\left(\frac{[^{188}Os]}{[Os]}\right)_{riv} + F_{hyd}\left(\frac{[^{188}Os]}{[Os]}\right)_{hyd} + F_{ext}\left(\frac{[^{188}Os]}{[Os]}\right)_{ext} - F_{sed}\left(\frac{[^{188}Os]}{[Os]}\right)_{sed} \quad (17)$$

where F represents the fluxes of Os (in mol / yr) from and to various reservoirs and the subscripts *sw, riv, hyd, ext* and *sed* represent seawater, riverine, hydrothermal, extraterrestrial and sediment reservoirs, respectively[14,83].

Substituting equations (3) and (4) into equations (16) and (17), respectively, yields:

$$\frac{d^{187}N}{dt} = F_{riv}\,\frac{R_{riv}}{7.4+R_{riv}} + F_{hyd}\,\frac{R_{hyd}}{7.4+R_{hyd}} + F_{ext}\,\frac{R_{ext}}{7.4+R_{ext}} - F_{sed}\,\frac{R_{sed}}{7.4+R_{sed}} \quad (18)$$

$$\frac{d^{188}N}{dt} = F_{riv}\,\frac{1}{7.4+R_{riv}} + F_{hyd}\,\frac{1}{7.4+R_{hyd}} + F_{ext}\,\frac{1}{7.4+R_{ext}} - F_{sed}\,\frac{1}{7.4+R_{sed}} \quad (19)$$

Finally, substituting equations (18) and (19) into equation (14) and combining with equation (4) results in:

$$\frac{N}{7.4+R_{\mathrm{sw}}}\frac{dR_{\mathrm{sw}}}{dt} = F_{\mathrm{riv}}\frac{R_{\mathrm{riv}}-R_{\mathrm{sw}}}{7.4+R_{\mathrm{riv}}} + F_{\mathrm{hyd}}\frac{R_{\mathrm{hyd}}-R_{\mathrm{sw}}}{7.4+R_{\mathrm{hyd}}} + F_{\mathrm{ext}}\frac{R_{\mathrm{ext}}-R_{\mathrm{sw}}}{7.4+R_{\mathrm{ext}}} - F_{\mathrm{sed}}\frac{R_{\mathrm{sed}}-R_{\mathrm{sw}}}{7.4+R_{\mathrm{sed}}} \quad (20)$$

which relates changes in R_{sw} over time to the fluxes of total Os (F), the $^{187}Os/^{188}Os$ compositions of these fluxes (R) and the amount of total Os in the ocean (N). Because there is no isotopic fractionation associated with Os burial (i.e., $R_{sed} = R_{sw}$), the net effect of the sedimentary Os flux (F_{sed}) in equation (20) is zero.

Together, equations (15) and (20) can be used to simulate any transient perturbation of the Os cycle. We first constructed a steady state model based on flux estimates and $^{187}Os/^{188}Os$ values for the present-day Os cycle with a $^{187}Os/^{188}Os$ ratio of seawater of 1.06 (see Supplementary Table 5). For the middle Eocene Os cycle, we assumed that the total Os inventory and the total input and output fluxes of Os are similar to present-day values, and recalculated the steady state riverine and hydrothermal Os fluxes for the pre-MECO $^{187}Os/^{188}Os$ ratio of seawater of 0.55 by assuming that the $^{187}Os/^{188}Os$ composition of these fluxes has remained unchanged. Subsequently, we used scaled silicate weathering and volcanic degassing fluxes from the LOSCAR model simulations to force our model of the Os cycle. The modeled changes in the $^{187}Os/^{188}Os$ ratio of seawater are included in the respective figures of all model scenarios (Fig. 3 of the main text and Supplementary Fig. 4 – 9). The full code used to perform the Os cycle model simulations is included as an R script in the Supplementary Software.

Data availability

The authors declare that all data supporting the results of this study are available in the Supplementary Information files associated with this manuscript.

514 **References**

515

516 1. Berner, R. A., Lasaga, A. C. & Garrels, R. M. The carbonate-silicate geochemical
517 cycle and its effect on atmospheric carbon dioxide over the past 100 million years. *Am.*
518 *J. Sci.* **283,** 641–683 (1983).

519 2. Walker, J. C. G., Hays, P. B. & Kasting, J. F. A negative feedback mechanism for the
520 long-term stabilization of Earth's surface temperature. *J. Geophys. Res.* **86,** 9776–9782
521 (1981).

522 3. Ravizza, G. E., Norris, R. N., Blusztajn, J. & Aubry, M.-P. An osmium isotope
523 excursion associated with the late Paleocene thermal maximum: Evidence of
524 intensified chemical weathering. *Paleoceanography* **16,** 155–163 (2001).

525 4. Pogge von Strandmann, P. A. E., Jenkyns, H. C. & Woodfine, R. G. Lithium isotope
526 evidence for enhanced weathering during Oceanic Anoxic Event 2. *Nat. Geosci.* **6,**
527 668–672 (2013).

528 5. Cohen, A. S., Coe, A. L., Harding, S. M. & Schwark, L. Osmium isotope evidence for
529 the regulation of atmospheric CO_2 by continental weathering. *Geology* **32,** 157–160
530 (2004).

531 6. Vance, D., Teagle, D. A. H. & Foster, G. L. Variable Quaternary chemical weathering
532 fluxes and imbalances in marine geochemical budgets. *Nature* **458,** 493–6 (2009).

533 7. Dickson, A. J. *et al.* Evidence for weathering and volcanism during the PETM from
534 Arctic Ocean and Peri-Tethys osmium isotope records. *Palaeogeogr. Palaeoclimatol.*
535 *Palaeoecol.* **438,** 300–307 (2015).

536 8. Sluijs, A., Zeebe, R. E., Bijl, P. K. & Bohaty, S. M. A middle Eocene carbon cycle
537 conundrum. *Nat. Geosci.* **6,** 429–434 (2013).

538 9. Bohaty, S. M. & Zachos, J. C. Significant Southern Ocean warming event in the late

539 middle Eocene. *Geology* **31,** 1017 (2003).
540 10. Bohaty, S. M., Zachos, J. C., Florindo, F. & Delaney, M. L. Coupled greenhouse
541 warming and deep-sea acidification in the middle Eocene. *Paleoceanography* **24,**
542 (2009).
543 11. Bijl, P. K. *et al.* Transient Middle Eocene atmospheric CO_2 and temperature variations.
544 *Science* **330,** 819–821 (2010).
545 12. Boscolo Galazzo, F. *et al.* The Middle Eocene Climatic Optimum: a Multi-Proxy
546 Record of Paleoceanographic Changes in the South Atlantic (ODP Site 1263).
547 *Paleoceanography* **29,** 1143–1161 (2014).
548 13. Cramwinckel, M. J. *et al.* Synchronous tropical and polar temperature evolution in the
549 Eocene. *Nature* (in press).
550 14. Peucker-Ehrenbrink, B. & Ravizza, G. E. The marine osmium isotope record. *Terra*
551 *Nov.* **12,** 205–219 (2000).
552 15. Peucker-Ehrenbrink, B. & Ravizza, G. E. in *The Geologic Time Scale 2012 2-Volume*
553 *Set* 145–166 (Elsevier, 2012).
554 16. Rooney, A. D. *et al.* Tracking millennial-scale Holocene glacial advance and retreat
555 using osmium isotopes: Insights from the Greenland ice sheet. *Quat. Sci. Rev.* **138,** 49–
556 61 (2016).
557 17. Ravizza, G. E. & Turekian, K. K. The osmium isotopic composition of organic-rich
558 marine sediments. *Earth Planet. Sci. Lett.* **110,** 1–6 (1992).
559 18. Cohen, A. S., Coe, A. L., Bartlett, J. M. & Hawkesworth, C. J. Precise Re-Os ages of
560 organic-rich mudrocks and the Os isotope composition of Jurassic seawater. *Earth*
561 *Planet. Sci. Lett.* **167,** 159–173 (1999).
562 19. Ravizza, G. E. & Zachos, J. C. Records of Cenozoic Ocean Chemistry. *Treatise on*
563 *Geochemistry* **6,** 551–581 (2003).

20. Them, T. R. *et al.* Evidence for rapid weathering response to climatic warming during the Toarcian Oceanic Anoxic Event. *Sci. Rep.* **7,** 5003 (2017).

21. Ridgwell, A. & Zeebe, R. E. The role of the global carbonate cycle in the regulation and evolution of the Earth system. *Earth Planet. Sci. Lett.* **234,** 299–315 (2005).

22. Pälike, H. *et al.* A Cenozoic record of the equatorial Pacific carbonate compensation depth. *Nature* **488,** 609–614 (2012).

23. Zeebe, R. E. LOSCAR: Long-term Ocean-atmosphere-Sediment CArbon cycle Reservoir model v2.0.4. *Geosci. Model Dev.* **5,** 149–166 (2012).

24. Cohen, A. S. & Coe, A. L. New geochemical evidence for the onset of volcanism in the Central Atlantic magmatic province and environmental change at the Triassic-Jurassic boundary. *Geology* **30,** 267–270 (2002).

25. Ravizza, G. E. Osmium-isotope geochemistry of Site 959: implications for Re-Os sedimentary geochronology and reconstruction of past variations in the Os-isotopic composition of seawater. *Proc. Ocean Drill. Program, Sci. Results* **159,** 181–186 (1998).

26. Ravizza, G. E. & Paquay, F. S. Os isotope chemostratigraphy applied to organic-rich marine sediments from the Eocene-Oligocene transition on the West African margin (ODP Site 959). *Paleoceanography* **23,** (2008).

27. Klemm, V., Levasseur, S., Frank, M., Hein, J. R. & Halliday, A. N. Osmium isotope stratigraphy of a marine ferromanganese crust. *Earth Planet. Sci. Lett.* **238,** 42–48 (2005).

28. Burton, K. W. Global weathering variations inferred from marine radiogenic isotope records. *J. Geochemical Explor.* **88,** 262–265 (2006).

29. Nielsen, S. G. *et al.* Thallium isotope evidence for a permanent increase in marine organic carbon export in the early Eocene. *Earth Planet. Sci. Lett.* **278,** 297–307

(2009).

30. Paquay, F. S. & Ravizza, G. E. Heterogeneous seawater $^{187}Os/^{188}Os$ during the Late Pleistocene glaciations. *Earth Planet. Sci. Lett.* **349–350,** 126–138 (2012).

31. Du Vivier, A. D. C. *et al.* Marine $^{187}Os/^{188}Os$ isotope stratigraphy reveals the interaction of volcanism and ocean circulation during Oceanic Anoxic Event 2. *Earth Planet. Sci. Lett.* **389,** 23–33 (2014).

32. Elsworth, G., Galbraith, E., Halverson, G. & Yang, S. Enhanced weathering and CO_2 drawdown caused by latest Eocene strengthening of the Atlantic meridional overturning circulation. *Nat. Geosci.* (2017).

33. Ravizza, G. E. & Peucker-Ehrenbrink, B. Chemostratigraphic Evidence of Deccan Volcanism from the Marine Osmium Isotope Record. *Science* **302,** 1392–1395 (2003).

34. Turgeon, S. C. & Creaser, R. A. Cretaceous oceanic anoxic event 2 triggered by a massive magmatic episode. *Nature* **454,** 323–326 (2008).

35. Robinson, N., Ravizza, G. E., Coccioni, R., Peucker-Ehrenbrink, B. & Norris, R. D. A high-resolution marine $^{187}Os/^{188}Os$ record for the late Maastrichtian: Distinguishing the chemical fingerprints of Deccan volcanism and the KP impact event. *Earth Planet. Sci. Lett.* **281,** 159–168 (2009).

36. Henehan, M. J., Hull, P. M., Penman, D. E., Rae, J. W. B. & Schmidt, D. N. Biogeochemical significance of pelagic ecosystem function: an end-Cretaceous case study. *Philos. Trans. R. Soc. B Biol. Sci.* **371,** 20150510 (2016).

37. Kerrick, D. M. & Caldeira, K. Paleoatmospheric consequences of CO_2 released during early Cenozoic regional metamorphism in the Tethyan orogen. *Chem. Geol.* **108,** 201–230 (1993).

38. Kerrick, D. M. & Caldeira, K. Was the Himalayan orogen a climatically significant coupled source and sink for atmospheric CO_2 during the Cenozoic? *Earth Planet. Sci.*

Lett. **173,** 195–203 (1999).

39. Cambray, H. & Cadet, J.-P. Synchronisme de l'activité volcanique d'arc: mythe ou réalité? *Comptes rendus l'Académie des Sci. Série 2. Sci. la terre des planètes* **322,** 237–244 (1996).

40. McDowell, F. W. & Mauger, R. L. K-Ar and U-Pb zircon chronology of late Cretaceous and Tertiary magmatism in central Chihuahua State, Mexico. *Geol. Soc. Am. Bull.* **106,** 118–132 (1994).

41. Sigurdsson, H. *et al.* History of circum-Caribbean explosive volcanism: $^{40}Ar/^{39}Ar$ dating of tephra layers. *Proc. Ocean Drill. Program, Sci. Results* **165,** 299–314 (2000).

42. Aguirre-Díaz, G. J. & Labarthe-Hernández, G. Fissure ignimbrites: Fissure-source origin for voluminous ignimbrites of the Sierra Madre Occidental and its relationship with Basin and Range faulting. *Geology* **31,** 773–776 (2003).

43. Bailey, D. K. Episodic alkaline igneous activity across Africa: implications for the causes of continental break-up. *Geol. Soc. London, Spec. Publ.* **68,** 91–98 (1992).

44. George, R., Rogers, N. & Kelley, S. Earliest magmatism in Ethiopia: Evidence for two mantle plumes in one flood basalt province. *Geology* **26,** 923 (1998).

45. Rooney, T. O. The Cenozoic magmatism of East-Africa: Part I — Flood basalts and pulsed magmatism. *Lithos* **286–287,** 264–301 (2017).

46. Torsvik, T. H. & Cocks, L. R. M. Norway in space and time: A Centennial cavalcade. *Nor. Geol. Tidsskr.* **85,** 73–86 (2005).

47. Mjelde, R. *et al.* Magmatic and tectonic evolution of the North Atlantic. *J. Geol. Soc. London.* **165,** 31–42 (2008).

48. Torsvik, T. H. *et al.* Continental crust beneath southeast Iceland. *Proc. Natl. Acad. Sci.* **112,** E1818–E1827 (2015).

49. Singh, S. K., Trivedi, J. R. & Krishnaswami, S. Re-Os isotope systematics in black

shales from the Lesser Himalaya: Their chronology and role in the $^{187}Os/^{188}Os$ evolution of seawater. *Geochim. Cosmochim. Acta* **63,** 2381–2392 (1999).

50. Pierson-Wickmann, A. C., Reisberg, L. & France-Lanord, C. The Os isotopic composition of Himalayan river bedloads and bedrocks: Importance of black shales. *Earth Planet. Sci. Lett.* **176,** 203–218 (2000).

51. Sharma, M., Wasserburg, G. J., Hofmann, A. W. & Chakrapani, G. J. Himalayan uplift and osmium isotopes in oceans and rivers. *Geochim. Cosmochim. Acta* **63,** 4005–4012 (1999).

52. Paul, M. *et al.* Dissolved osmium in Bengal plain groundwater: Implications for the marine Os budget. *Geochim. Cosmochim. Acta* **74,** 3432–3448 (2010).

53. Anagnostou, E. *et al.* Changing atmospheric CO_2 concentration was the primary driver of early Cenozoic climate. *Nature* **533,** 380–384 (2016).

54. Luo, Y., Boudreau, B. P., Dickens, G. R., Sluijs, A. & Middelburg, J. J. An alternative model for $CaCO_3$ over-shooting during the PETM: Biological carbonate compensation. *Earth Planet. Sci. Lett.* **453,** 223–233 (2016).

55. Spofforth, D. J. A. *et al.* Organic carbon burial following the middle Eocene climatic optimum in the central western Tethys. *Paleoceanography* **25,** (2010).

56. Maher, K. & Chamberlain, C. P. Hydrologic Regulation of Chemical Weathering and the Geologic Carbon Cycle. *Science* **343,** 1502–1504 (2014).

57. Caves, J. K., Jost, A. B., Lau, K. V. & Maher, K. Cenozoic carbon cycle imbalances and a variable weathering feedback. *Earth Planet. Sci. Lett.* **450,** 152–163 (2016).

58. Kump, L. R. & Arthur, M. A. in *Tectonic Uplift and Climate Change* (ed. Ruddiman, W.) 399–426 (Plenum Publishing Co., 1997).

59. Kump, L. R., Brantley, S. L. & Arthur, M. A. Chemical weathering, atmospheric CO_2, and climate. *Annu. Rev. Earth Planet. Sci.* **28,** 611–667 (2000).

60. Zachos, J. C., Dickens, G. R. & Zeebe, R. E. An early Cenozoic perspective on greenhouse warming and carbon-cycle dynamics. *Nature* **451,** 279–283 (2008).

61. West, A. J., Galy, A. & Bickle, M. J. Tectonic and climatic controls on silicate weathering. *Earth Planet. Sci. Lett.* **235,** 211–228 (2005).

62. Froelich, P. N. & Misra, S. Was the Late Paleocene-Early Eocene Hot Because Earth Was Flat? An Ocean Lithium Isotope View of Mountain Building, Continental Weathering, Carbon Dioxide, and Earth's Cenozoic climate. *Oceanography* **27,** 36–49 (2014).

63. Kump, L. R. *et al.* A weathering hypothesis for glaciation at high atmospheric pCO_2 during the Late Ordovician. *Palaeogeogr. Palaeoclimatol. Palaeoecol.* **152,** 173–187 (1999).

64. Mills, B., Watson, A. J., Goldblatt, C., Boyle, R. & Lenton, T. M. Timing of Neoproterozoic glaciations linked to transport-limited global weathering. *Nat. Geosci.* **4,** 861–864 (2011).

65. Goddéris, Y. *et al.* Onset and ending of the late Palaeozoic ice age triggered by tectonically paced rock weathering. *Nat. Geosci.* **10,** 382–386 (2017).

66. Wagner, T. Late Cretaceous to early Quaternary organic sedimentation in the eastern Equatorial Atlantic. *Palaeogeogr. Palaeoclimatol. Palaeoecol.* **179,** 113–147 (2002).

67. Selby, D. & Creaser, R. A. Re–Os geochronology of organic rich sediments: an evaluation of organic matter analysis methods. *Chem. Geol.* **200,** 225–240 (2003).

68. Li, C., Qu, W. J., Du, A. D. & Sun, W. Comprehensive study on extraction of rhenium with acetone in Re-Os isotopic dating. *Rock Miner. Anal.* **28,** 233–238 (2009).

69. Cumming, V. M., Selby, D. & Lillis, P. G. Re-Os geochronology of the lacustrine Green River Formation: Insights into direct depositional dating of lacustrine successions, Re-Os systematics and paleocontinental weathering. *Earth Planet. Sci.*

Lett. **359–360,** 194–205 (2012).

70. Smoliar, M. I., Walker, R. J. & Morgan, J. W. Re-Os Ages of Group IIA, IIIA, IVA, and IVB Iron Meteorites. *Science* **271,** 1099–1102 (1996).

71. Shafik, S., Watkins, D. K. & Shin, I. C. Calcareous Nannofossil Paleogene Biostratigraphy, Côte D'Ivoire-Ghana Marginal Ridge, Eastern Equatorial Atlantic. *Proc. Ocean Drill. Program, Sci. Results* **159,** 413–431 (1998).

72. Pälike, H. *et al.* The heartbeat of the Oligocene climate system. *Science* **314,** 1894–1898 (2006).

73. Toffanin, F., Agnini, C., Rio, D., Acton, G. & Westerhold, T. Middle Eocene to early Oligocene calcareous nannofossil biostratigraphy at IODP Site U1333 (equatorial Pacific). *Micropaleontology* **59,** 69–82 (2013).

74. Gradstein, F. M., Ogg, J. G., Schmitz, M. & Ogg, G. *The Geologic Time Scale 2012 2-Volume Set*. (Elsevier, 2012).

75. Pegram, W. J. & Turekian, K. K. The osmium isotopic composition change of Cenozoic sea water as inferred from a deep-sea core corrected for meteoritic contributions. *Geochim. Cosmochim. Acta* **63,** 4053–4058 (1999).

76. Peucker-Ehrenbrink, B. Accretion of extraterrestrial matter during the last 80 million years and its effect on the marine osmium isotope record. *Geochim. Cosmochim. Acta* **60,** 3187–3196 (1996).

77. Faure, G. *Principles of Isotope Geology*. (Wiley, 1986).

78. Li, G. & Elderfield, H. Evolution of carbon cycle over the past 100 million years. *Geochim. Cosmochim. Acta* **103,** 11–25 (2013).

79. Meisel, T., Walker, R. J., Irving, A. J. & Lorand, J. P. Osmium isotopic compositions of mantle xenoliths: A global perspective. *Geochim. Cosmochim. Acta* **65,** 1311–1323 (2001).

80. Martin, C. E. Osmium isotopic characteristics of mantle-derived rocks. *Geochim. Cosmochim. Acta* **55,** 1421–1434 (1991).

81. Hauff, F., Hoernle, K., Tilton, G., Graham, D. W. & Kerr, A. C. Large volume recycling of oceanic lithosphere over short time scales: Geochemical constraints from the Caribbean Large Igneous Province. *Earth Planet. Sci. Lett.* **174,** 247–263 (2000).

82. Walker, J. C. G. & Kasting, J. F. Effects of fuel and forest conservation on future levels of atmospheric carbon dioxide. *Palaeogeogr. Palaeoclimatol. Palaeoecol.* **97,** 151–189 (1992).

83. Richter, F. M. & Turekian, K. K. Simple models for the geochemical response of the ocean to climatic and tectonic forcing. *Earth Planet. Sci. Lett.* **119,** 121–131 (1993).

84. Westerhold, T. *et al.* Orbitally tuned timescale and astronomical forcing in the middle Eocene to early Oligocene. *Clim. Past* **10,** 955–973 (2014).

Acknowledgements

This research used samples provided by the Ocean Drilling Program (ODP) and Integrated Ocean Drilling Program (IODP). This work was carried out under the program of the Netherlands Earth System Science Centre (NESSC), which is financially supported by the Ministry of Education, Culture and Science (OCW) of the Netherlands. D.S. acknowledges support of the Total endowment fund and the Dida Scholarship of CUG Wuhan. Y.L. thanks Alan Rooney (Yale University) for intellectual freedom and a grant (SKL-K201706) from the Institute of Geology and Geophysics, Chinese Academy of Sciences. We thank Richard Zeebe (University of Hawai'i) for discussions on LOSCAR modeling, Antonia Hofmann, Geoff Nowell and Chris Ottley (Durham University) and Natasja Welters and Arnold van Dijk (Utrecht Geolab) for laboratory assistance, and Andy Ridgwell and two anonymous reviewers for constructive comments that significantly improved the manuscript.

Author contributions

R.v.d.P., S.M.B., J.J.M. and A.S. designed the study. R.v.d.P. and D.S. generated the osmium isotope records, M.J.C. performed the carbon cycle simulations, R.v.d.P. and Y. L. conducted the osmium cycle modeling and all authors contributed to data interpretation. R.v.d.P. wrote the manuscript with input from all authors.

Additional information

Correspondence should be addressed to R.v.d.P. (r.vanderploeg@uu.nl).

Competing financial interests

The authors declare no competing financial interests.

Figures

Figure 1: Os_i values (in blue) and ^{192}Os content (in red) for the analyzed middle Eocene sediments from the three different sites. a, ODP Site 959; **b**, ODP Site 1263; **c**, IODP Site U1333. The MECO extent is defined based on TEX_{86} values for Site 959 (in black; Cramwinckel et al., in press)[13] and bulk carbonate stable oxygen isotope ratios ($\delta^{18}O$) for Site 1263 (in black; Bohaty et al., 2009)[10]. The MECO is characterized by low carbonate content at Site U1333 (in grey; Westerhold et al., 2014)[84]. The error bars indicate fully propagated analytical uncertainties (2σ).

762 **Figure 2: Comparison of Os_i records from the MECO with Os_i records from the PETM**
763 **and ETM2, shown against the overall Os_i evolution of the Cenozoic and the relative**
764 **weathering feedback strength of the Cenozoic. a**, MECO data from Site 959 (in red), Site
765 1263 (in blue) and Site U1333 (in green) plotted against age (GTS2012)[74]. See Methods for
766 discussion of the age models for the study sites. **b**, MECO data from Sites 959, 1263 and
767 U1333 (this study); PETM and ETM2 data from DSDP Site 549 (in purple) as published in
768 Peucker-Ehrenbrink & Ravizza (2012)[15]; Cenozoic data from ferromanganese crusts D11 and
769 CD29 (in black) as published in Klemm et al. (2005)[27] and Burton (2006)[28], respectively,
770 based on the updated age model of Nielsen et al. (2009)[29]. **c,** Model estimates of the relative
771 continental weathering feedback strength of the Cenozoic as published in Caves et al.
772 (2016)[57], based on their CO_2 scenario 1 and a logarithmic expression for the weathering
773 feedback.
774

Figure 3: LOSCAR and Os cycle model simulations of the most likely MECO scenario. **a,** Forcing for two scenarios involving a gradual, transient 20 % increase in the volcanic CO_2 flux over ~500 kyr. The solid lines represent a scenario in which the silicate and carbonate weathering fluxes are allowed to vary in response to CO_2 forcing (normal weathering feedback), while the dashed lines represent a scenario in which these weathering fluxes are kept constant (diminished weathering feedback). Only the latter scenario corresponds to all observations. **b,** Model response in the $^{187}Os/^{188}Os$ composition of the global ocean, shown against smoothed fits to the MECO Os_i records from the study sites. **c,** Model CCD response of different ocean basins, shown against carbonate content (wt %) records for different depths in the Atlantic, Indian and Pacific oceans as compiled by Sluijs et al. (2013)[8]. **d,** Model atmospheric pCO_2 response and pH response for the surface Atlantic and Pacific oceans. **e,** Model $\delta^{13}C$ response for the DIC of the deep Atlantic and Pacific oceans. For a full description of the LOSCAR model, see Zeebe (2012)[23].

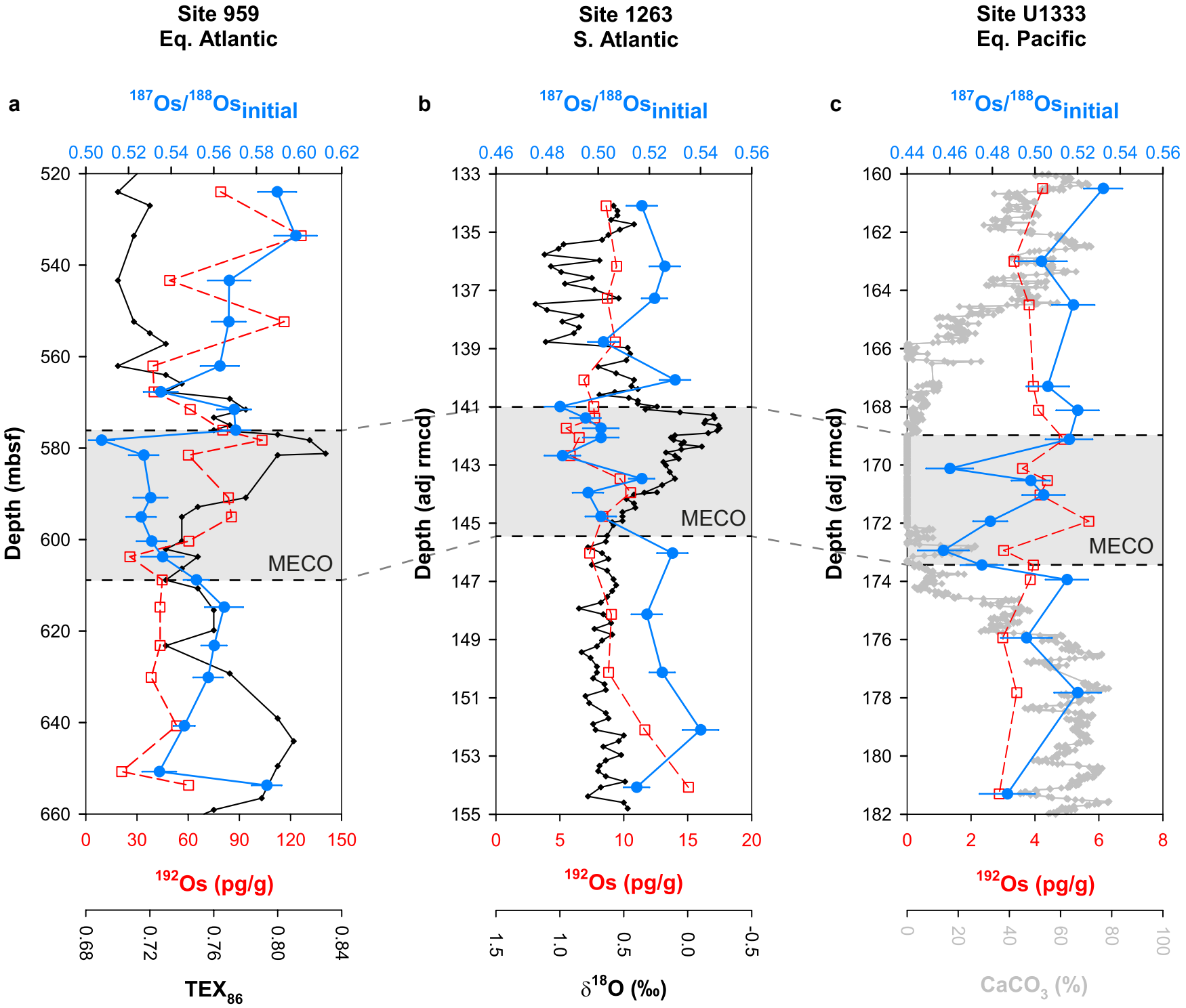
Site 959
Eq. Atlantic
Site 1263
S. Atlantic
Site U1333
Eq. Pacific
a
b
c
$^{187}Os/^{188}Os_{initial}$
0.50 0.52 0.54 0.56 0.58 0.60 0.62
0.46 0.48 0.50 0.52 0.54 0.56
0.44 0.46 0.48 0.50 0.52 0.54 0.56
Depth (mbsf)
Depth (adj rmcd)
MECO
520 540 560 580 600 620 640 660
133 135 137 139 141 143 145 147 149 151 153 155
160 162 164 166 168 170 172 174 176 178 180 182
0 30 60 90 120 150
0 5 10 15 20
0 2 4 6 8
^{192}Os (pg/g)
0.68 0.72 0.76 0.80 0.84
TEX$_{86}$
1.5 1.0 0.5 0.0 -0.5
$\delta^{18}O$ (‰)
0 20 40 60 80 100
$CaCO_3$ (%)

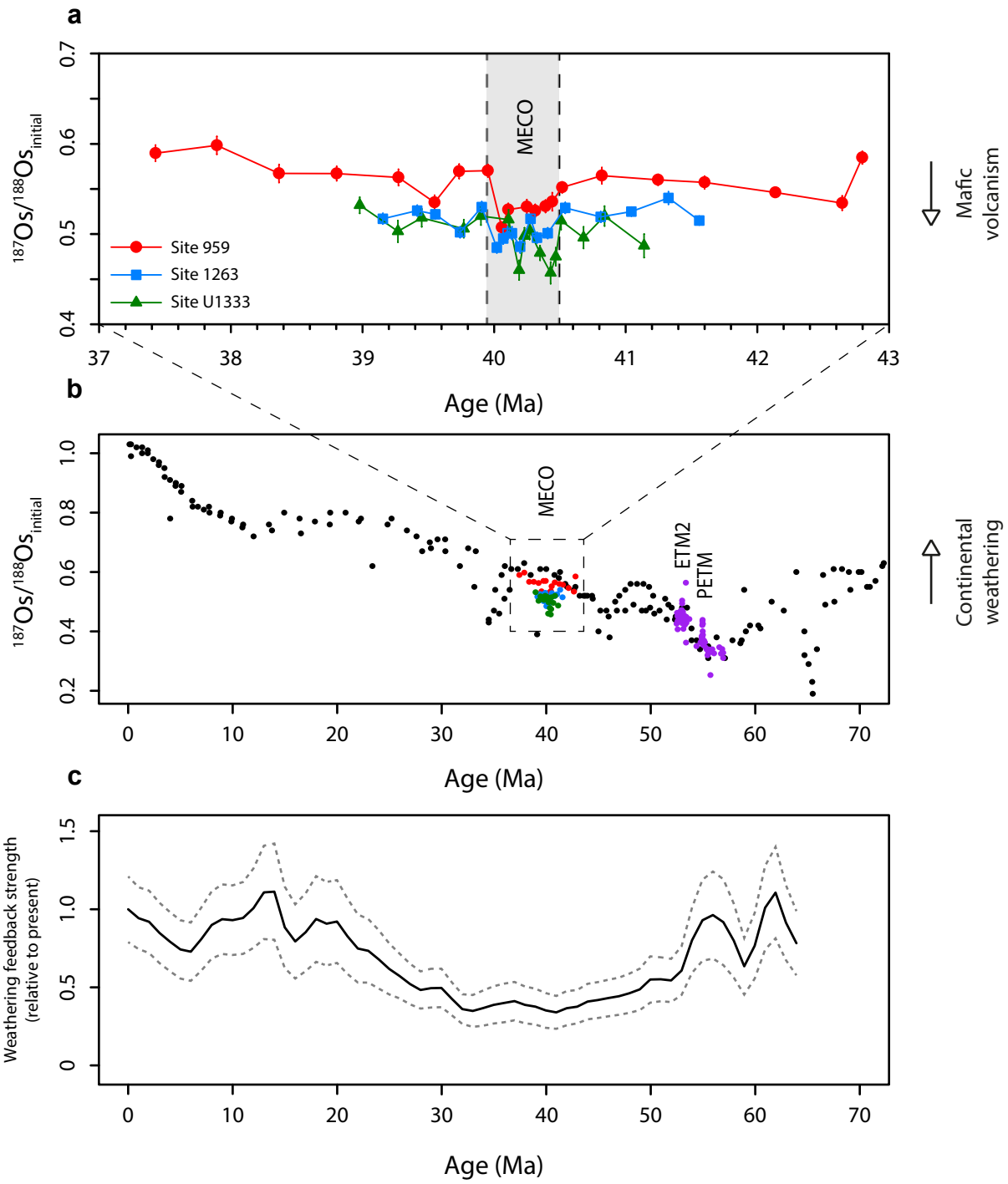
a
$^{187}Os/^{188}Os_{initial}$
0.7
0.6
0.5
0.4
MECO
Site 959
Site 1263
Site U1333
37
38
39
40
41
42
43
Age (Ma)
Mafic volcanism
b
$^{187}Os/^{188}Os_{initial}$
1.0
0.8
0.6
0.4
0.2
MECO
ETM2
PETM
0
10
20
30
40
50
60
70
Age (Ma)
Continental weathering
c
Weathering feedback strength (relative to present)
1.5
1.0
0.5
0
0
10
20
30
40
50
60
70
Age (Ma)

a

Volcanic degassing

Forcing (fluxes relative to initial values)

Model time (kyr)

b

Model $^{187}Os/^{188}Os_{sw}$

$^{187}Os/^{188}Os_{sw}$

$^{187}Os/^{188}Os_{initial}$

Age (Ma)

Model time (kyr)

Site 959 $^{187}Os/^{188}Os_{initial}$

Site 1263 $^{187}Os/^{188}Os_{initial}$

Site U1333 $^{187}Os/^{188}Os_{initial}$

c

Model CCD Tethys

Model CCD Pacific

Model CCD Indian

Model CCD Atlantic

CCD (m)

Age (Ma)

Model time (kyr)

Carbonate content at paleo-water depth (m)

10-20 30-40 50-60

0-10 20-30 40-50

$CaCO_3$ (%) Pacific

$CaCO_3$ (%) Indian

$CaCO_3$ (%) Atlantic

70-80 90-100

60-70 80-90

d

Model pCO_2 atmosphere

pCO_2 (ppmv)

Model time (kyr)

pH

Model pH surface Pacific

Model pH surface Atlantic

e

Model $\delta^{13}C$ deep Atlantic

Model $\delta^{13}C$ deep Pacific

$\delta^{13}C$ (‰)

Model time (kyr)

Middle Eocene greenhouse warming facilitated by diminished weathering feedback

Van der Ploeg et al.

Supplementary Information

This PDF file includes:

- Supplementary Figures 1 – 11
- Supplementary Tables 1 – 5
- Supplementary References 1 – 18

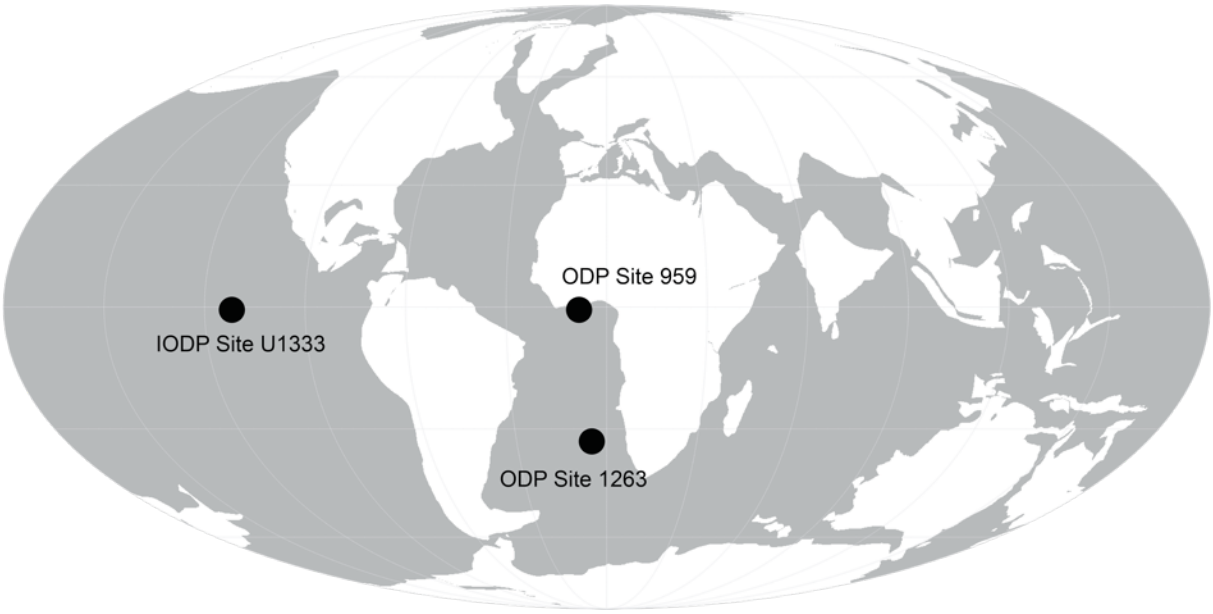

Supplementary Figure 1: Paleogeographic reconstruction of 40 Ma showing the estimated locations of the study sites. Shown are ODP Site 959 in the equatorial Atlantic along the African continent, ODP Site 1263 on the Walvis Ridge in the south Atlantic and IODP Site U1333 in the equatorial Pacific. The map was made with GPlates, based on the tectonic reconstructions of Seton et al. (2012)[1] and the paleomagnetic reference frame of Torsvik et al. (2012)[2].

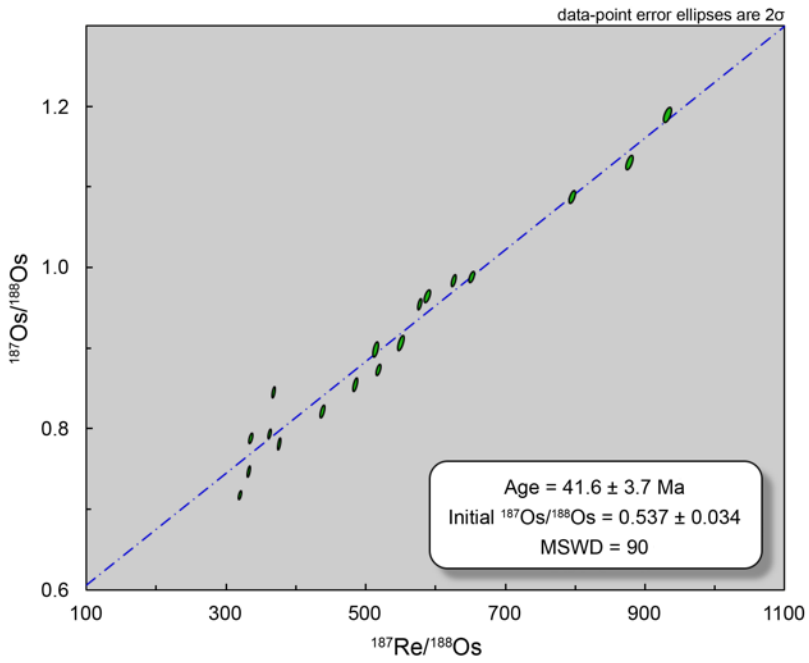

Supplementary Figure 2: Re-Os isochron plot of all Site 959 samples. The significant scatter (MSWD = 90) is best explained by the sample set possessing slightly variable initial $^{187}Os/^{188}Os$ compositions and being deposited over a prolonged interval of time (i.e., several Myr).

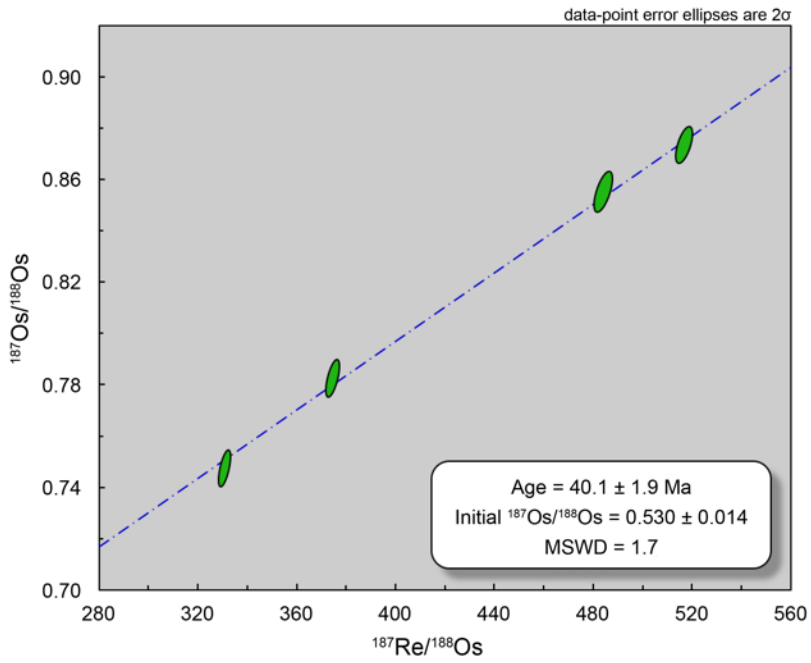

Supplementary Figure 3: Re-Os isochron plot of Site 959 samples in the MECO interval between 600.35 and 581.51 mbsf. These samples were selected because they were deposited in a short time interval (i.e., ~500 kyr), and yield virtually identical initial $^{187}Os/^{188}Os$ compositions. The obtained isochron age of 40.1 Ma is in excellent agreement with the estimated ages of these samples – between 40.4 and 40.1 Ma – based on our age model for Site 959.

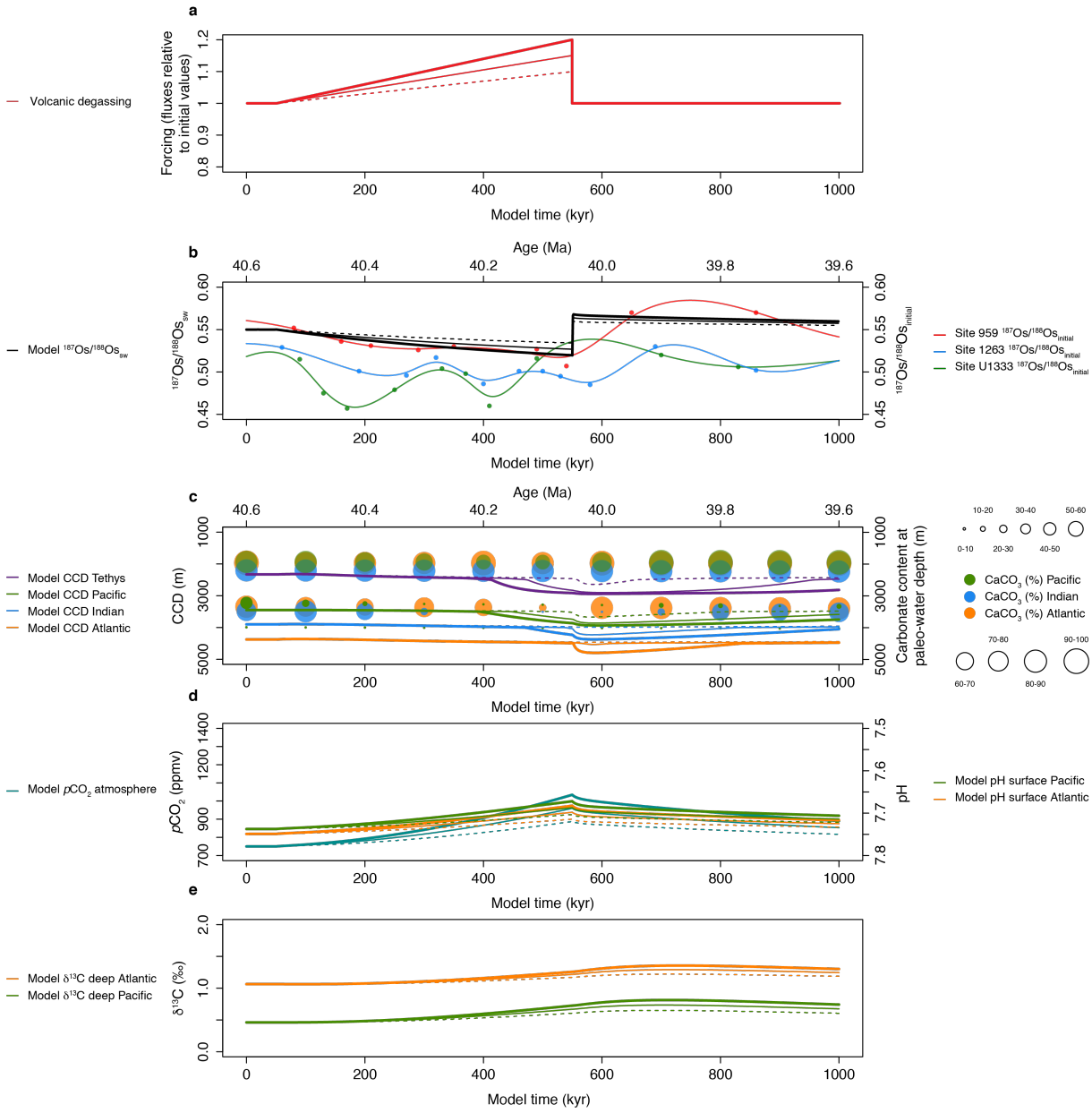

Supplementary Figure 4: LOSCAR and Os cycle model simulations of the MECO. a, Forcing for three scenarios involving a transient increase in the volcanic CO_2 flux of 10% (dashed lines), 15% (thin solid lines) and 20% (thick solid lines) over ~500 kyr, while allowing the silicate and carbonate weathering fluxes to vary as a feedback response. **b,** Model response in the $^{187}Os/^{188}Os$ composition of the global ocean, shown against smoothed fits to the MECO Os_i records from the study sites. **c,** Model CCD response of different ocean basins, shown against carbonate content (wt %) records for different depths in the Atlantic, Indian and Pacific oceans as compiled by Sluijs et al. (2013)[3]. **d,** Model atmospheric pCO_2 response and pH response for the surface Atlantic and Pacific oceans. **e,** Model $\delta^{13}C$ response for the DIC of the deep Atlantic and Pacific oceans.

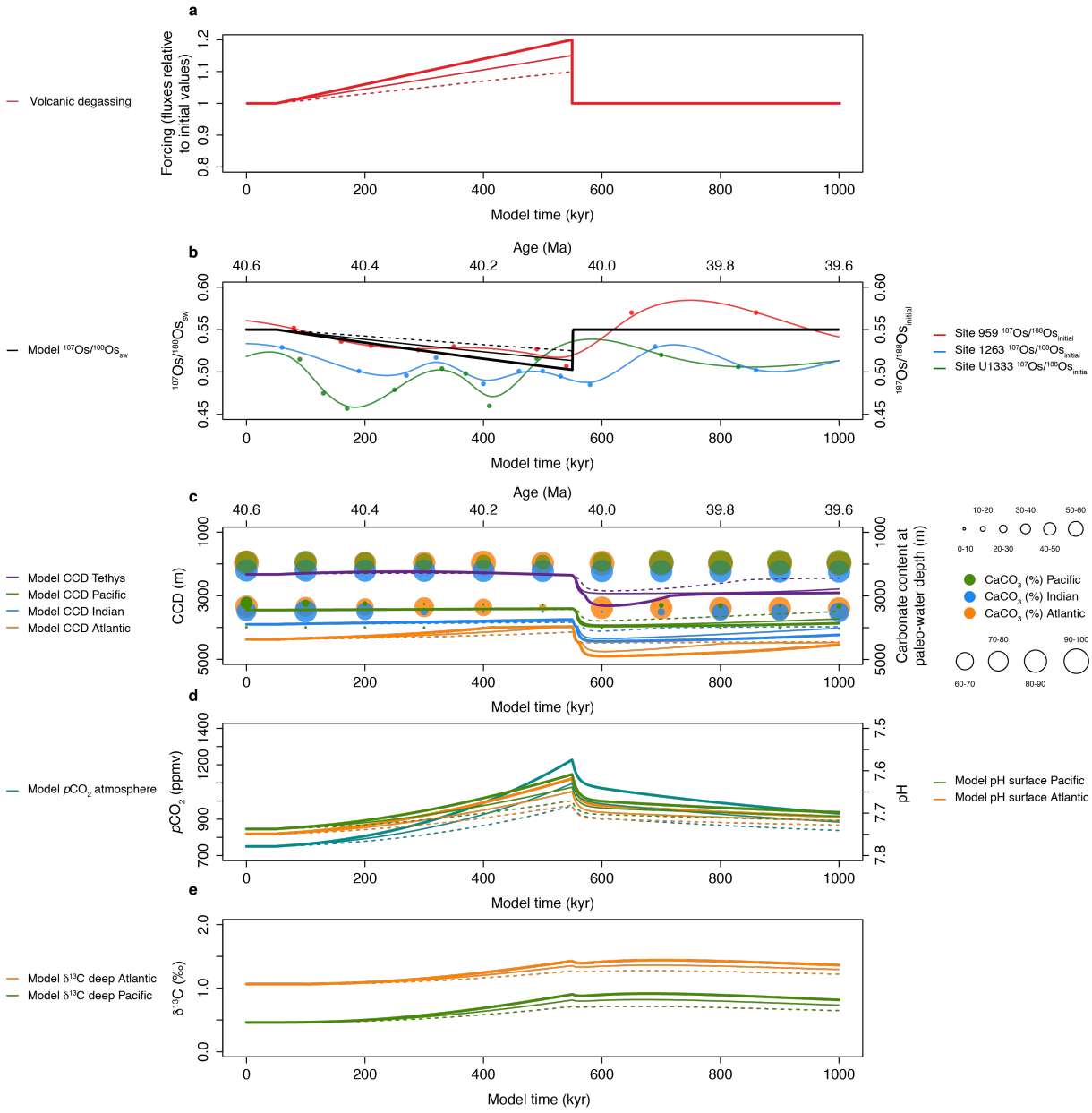

Supplementary Figure 5: LOSCAR and Os cycle model simulations of the MECO. a, Forcing for three scenarios involving a transient increase in the volcanic CO_2 flux of 10% (dashed lines), 15% (thin solid lines) and 20% (thick solid lines) over ~500 kyr, while maintaining the silicate and carbonate weathering fluxes at constant value. **b,** Model response in the $^{187}Os/^{188}Os$ composition of the global ocean, shown against smoothed fits to the MECO Os_i records from the study sites. **c,** Model CCD response of different ocean basins, shown against carbonate content (wt %) records for different depths in the Atlantic, Indian and Pacific oceans as compiled by Sluijs et al. (2013)[3]. **d,** Model atmospheric pCO_2 response and pH response for the surface Atlantic and Pacific oceans. **e,** Model $\delta^{13}C$ response for the DIC of the deep Atlantic and Pacific oceans.

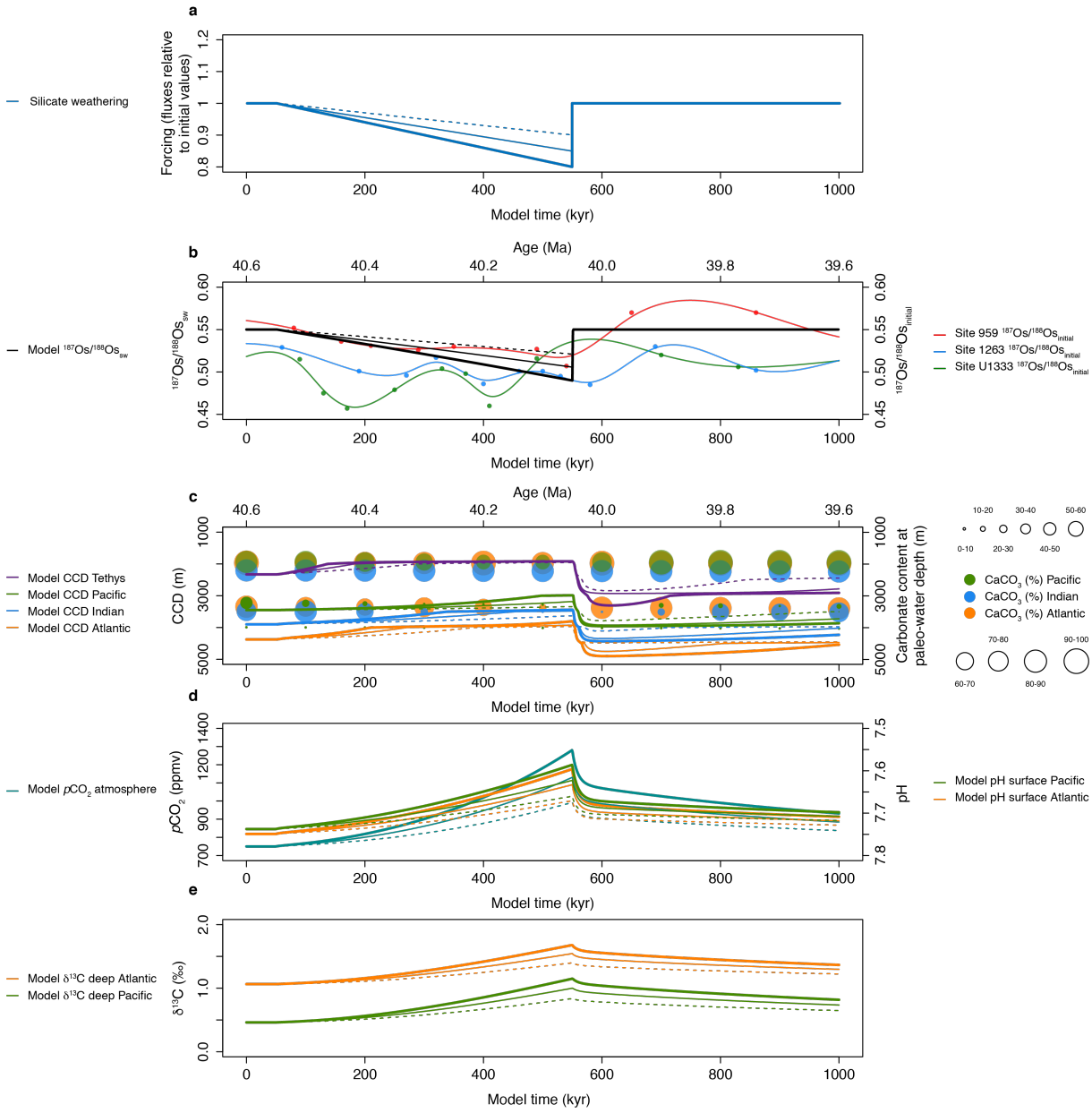

Supplementary Figure 6: LOSCAR and Os cycle model simulations of the MECO. a, Forcing for three scenarios involving a transient decrease in the silicate weathering flux of 10% (dashed lines), 15% (thin solid lines) and 20% (thick solid lines) over ~500 kyr, while keeping the volcanic CO_2 flux and the carbonate weathering flux at constant value. **b,** Model response in the $^{187}Os/^{188}Os$ composition of the global ocean, shown against smoothed fits to the MECO Os_i records from the study sites. **c,** Model CCD response of different ocean basins, shown against carbonate content (wt %) records for different depths in the Atlantic, Indian and Pacific oceans as compiled by Sluijs et al. (2013)[3]. **d,** Model atmospheric pCO_2 response and pH response for the surface Atlantic and Pacific oceans. **e,** Model $\delta^{13}C$ response for the DIC of the deep Atlantic and Pacific oceans.

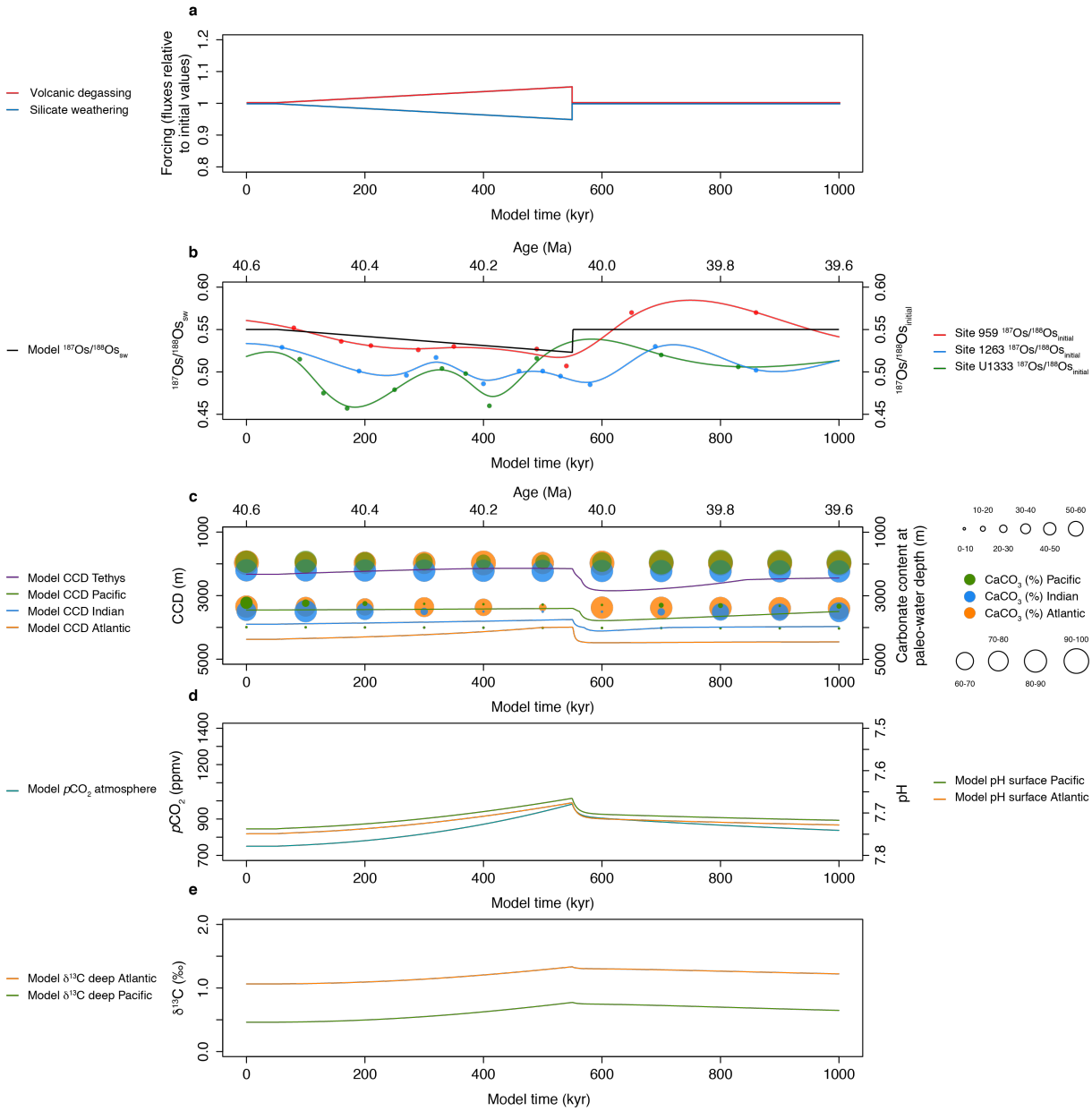

Supplementary Figure 7: LOSCAR and Os cycle model simulations of the MECO. a, Forcing for a scenario involving a transient 5% increase in the volcanic CO_2 flux combined with a 5% decrease in the silicate weathering flux over ~500 kyr, while keeping the carbonate weathering flux at constant value. **b,** Model response in the $^{187}Os/^{188}Os$ composition of the global ocean, shown against smoothed fits to the MECO Os_i records from the study sites. **c,** Model CCD response of different ocean basins, shown against carbonate content (wt %) records for different depths in the Atlantic, Indian and Pacific oceans as compiled by Sluijs et al. (2013)[3]. **d,** Model atmospheric pCO_2 response and pH response for the surface Atlantic and Pacific oceans. **e,** Model $\delta^{13}C$ response for the DIC of the deep Atlantic and Pacific oceans.

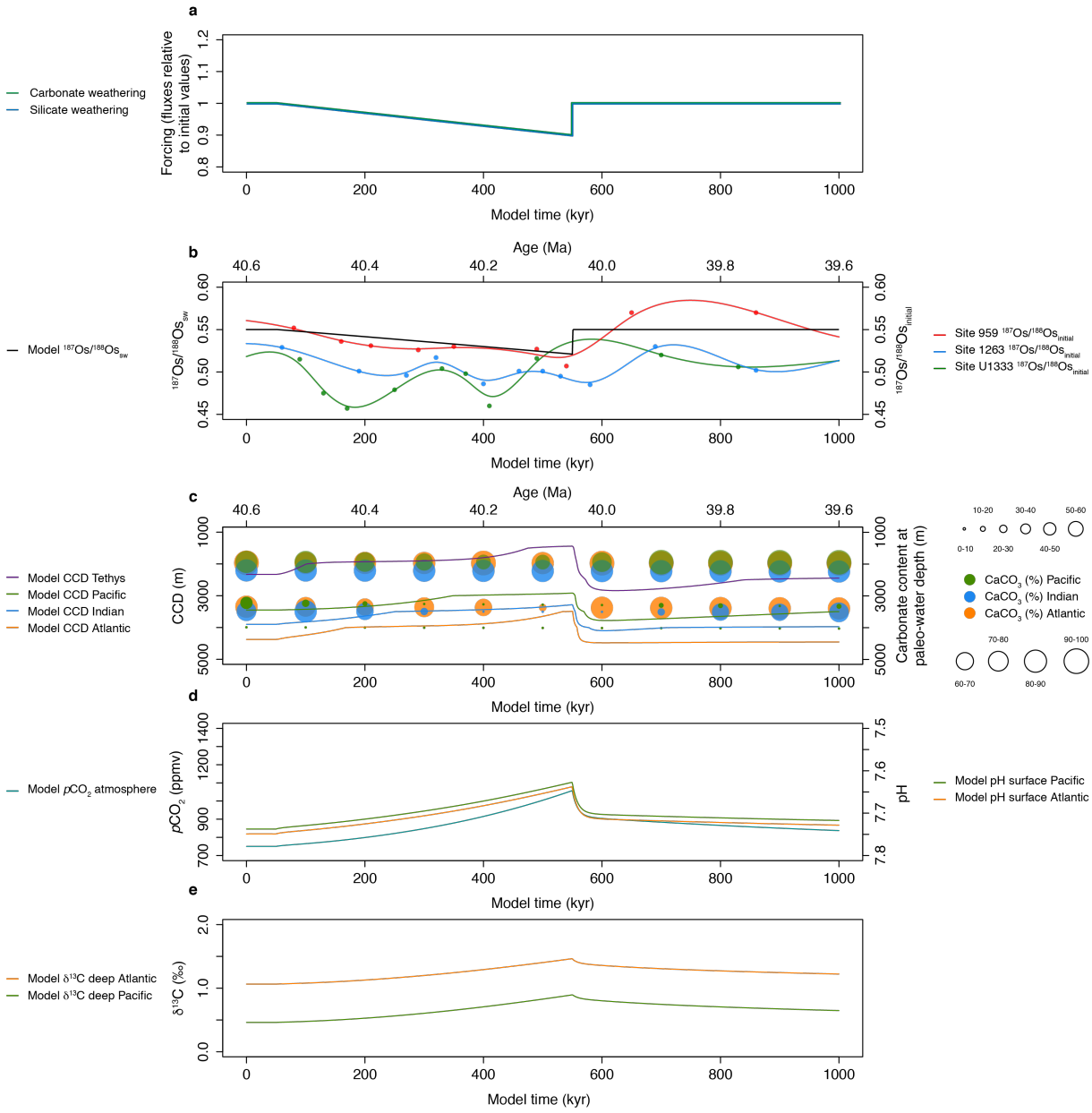

Supplementary Figure 8: LOSCAR and Os cycle model simulations of the MECO. a, Forcing for a scenario involving a transient, combined 10% decrease in the silicate and carbonate weathering fluxes over ~500 kyr, while keeping the volcanic CO_2 flux at constant value. **b,** Model response in the $^{187}Os/^{188}Os$ composition of the global ocean, shown against smoothed fits to the MECO Os_i records from the study sites. **c,** Model CCD response of different ocean basins, shown against carbonate content (wt %) records for different depths in the Atlantic, Indian and Pacific oceans as compiled by Sluijs et al. (2013)[3]. **d,** Model atmospheric pCO_2 response and pH response for the surface Atlantic and Pacific oceans. **e,** Model $\delta^{13}C$ response for the DIC of the deep Atlantic and Pacific oceans.

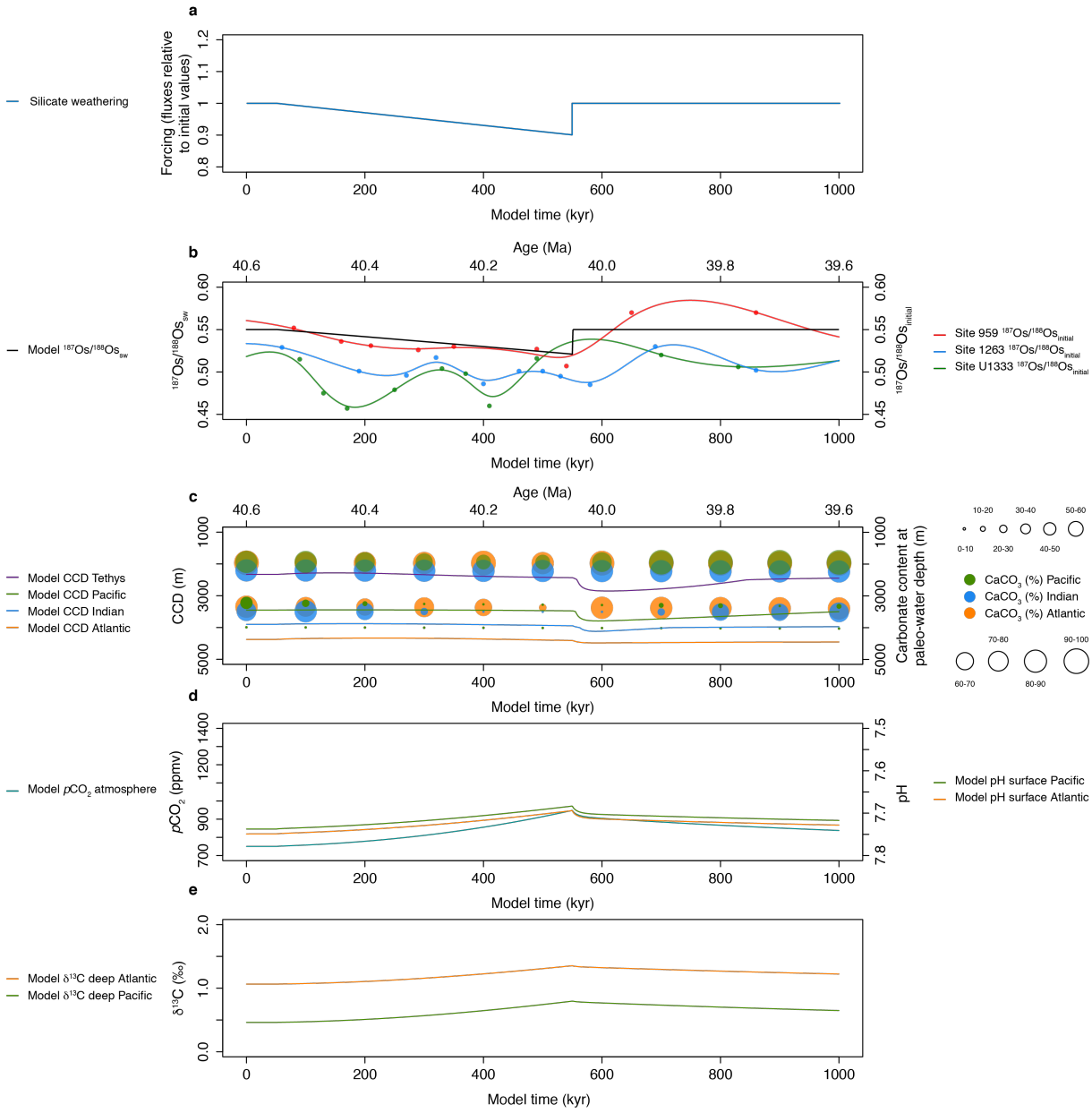

Supplementary Figure 9: LOSCAR and Os cycle model simulations of the MECO. a, Forcing for a scenario involving a transient 10% decrease in the silicate weathering flux over ~500 kyr, while keeping the volcanic CO_2 flux at constant value and allowing the carbonate weathering flux to vary as a feedback response. **b,** Model response in the $^{187}Os/^{188}Os$ composition of the global ocean, shown against smoothed fits to the MECO Os_i records from the study sites. **c,** Model CCD response of different ocean basins, shown against carbonate content (wt %) records for different depths in the Atlantic, Indian and Pacific oceans as compiled by Sluijs et al. (2013)[3]. **d,** Model atmospheric pCO_2 response and pH response for the surface Atlantic and Pacific oceans. **e,** Model $\delta^{13}C$ response for the DIC of the deep Atlantic and Pacific oceans.

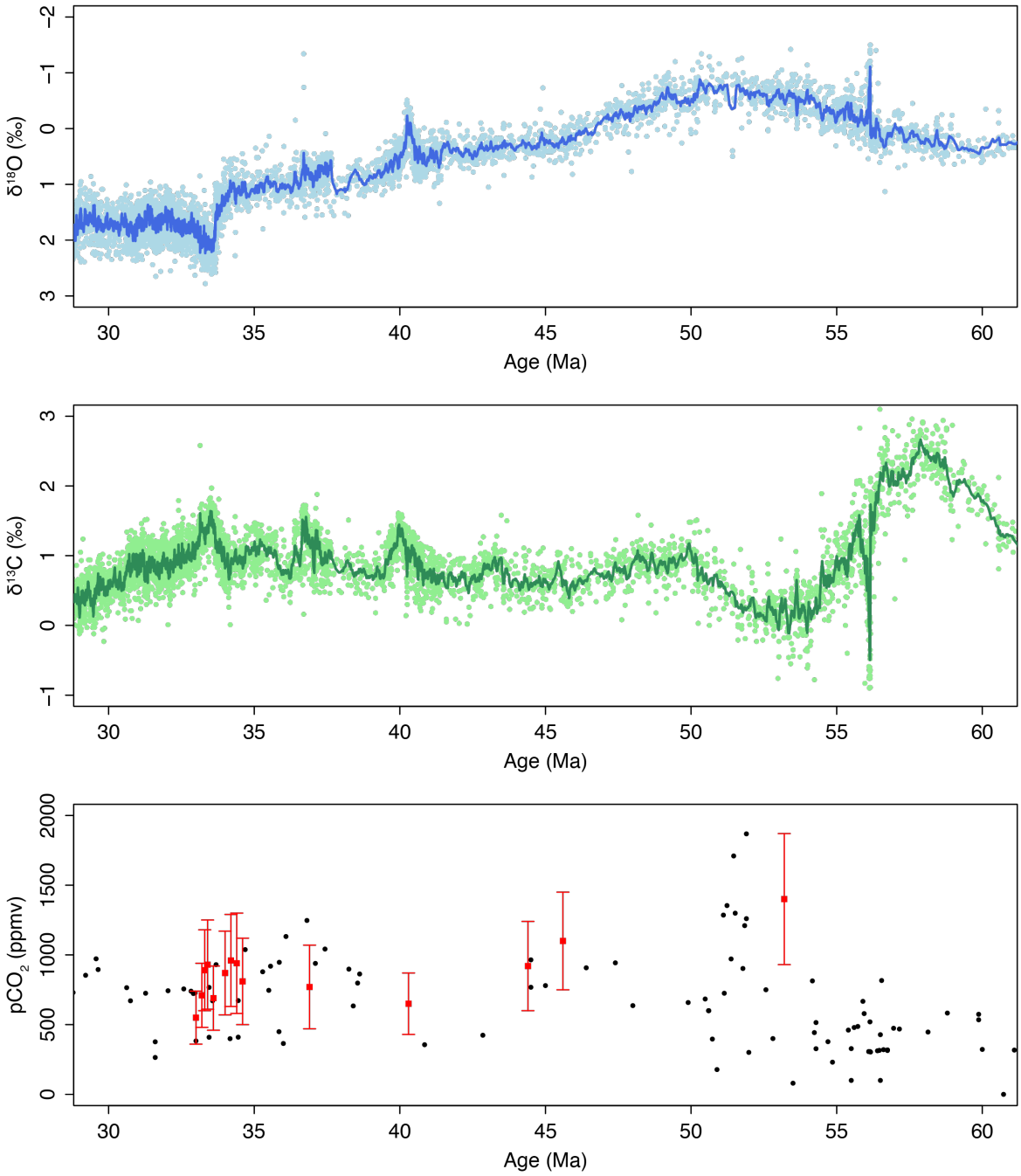

Supplementary Figure 10: Eocene trends in benthic foraminiferal $\delta^{18}O$ and $\delta^{13}C$, and atmospheric pCO_2. a, Benthic $\delta^{18}O$ compilation as published in Cramer et al. (2009)[4], adjusted to the framework of the GTS2012[5] and plotted as individual data points and as a 10-point running average (solid line). **b,** Benthic $\delta^{13}C$ compilation as published in Cramer et al. (2009)[4], adjusted to the framework of the GTS2012[5] and plotted as individual data points and as a 10-point running average (solid line). **c,** Atmospheric pCO_2 compilation as published in Foster et al. (2017)[6], with the $\delta^{11}B$-based pCO_2 estimates of Anagnostou et al. (2016)[7] highlighted in red.

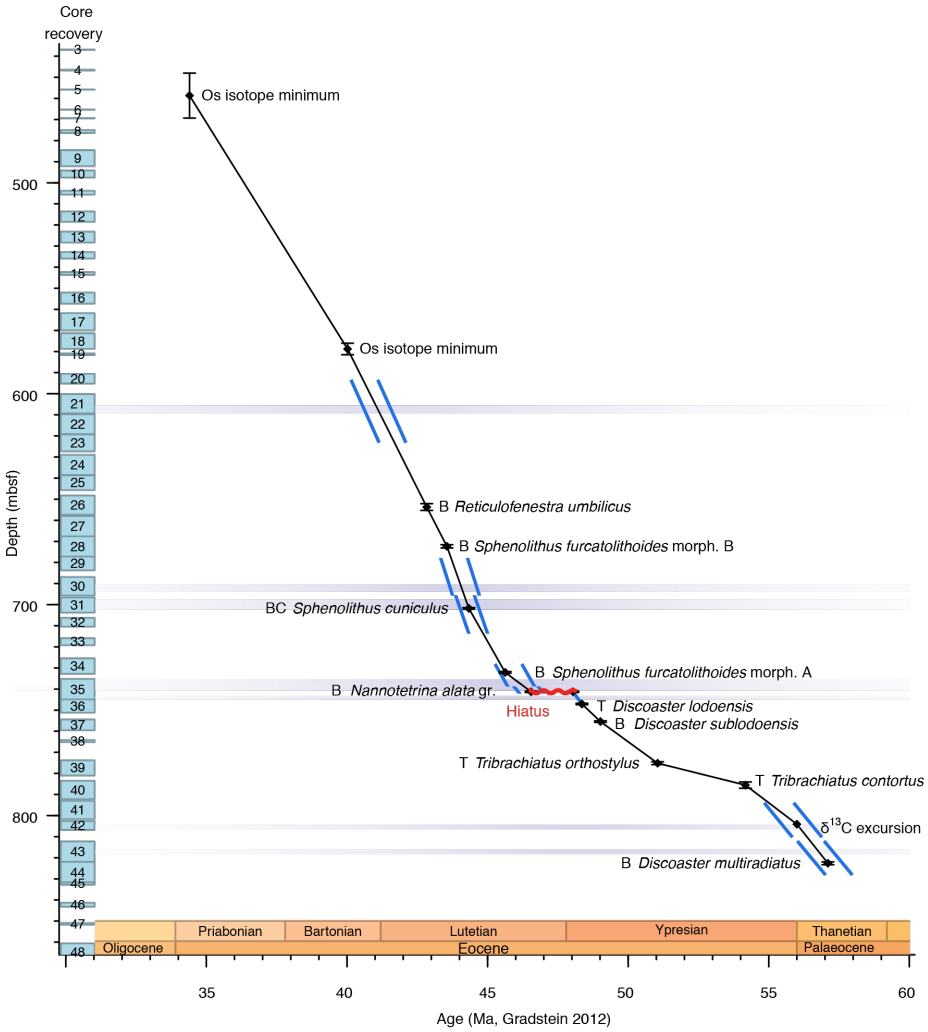

Supplementary Figure 11: Age model for Site 959 Hole D as presented in Cramwinckel et al. (2018)[8]. Diamonds with error bars show calcareous nannofossil and chemostratigraphic tie-points, adjusted to the framework of the GTS 2012[5]. The Os isotope minimum at ~40 Ma is derived from the MECO Os_i records presented in this study.

Supplementary Table 1: Age model for Site 959.

Stratigraphic datum	Depth (mbsf)	Age (Ma) [GTS 2004][9]	Age (Ma) [GTS 2012][5]	Source
$^{187}Os/^{188}Os$ minimum	466.6	34.5	34.65	Ravizza & Paquay (2008)[10]
TEX_{86} highest value at MECO peak	578.25	-	40.06	This study, based on Cramwinckel et al. (2018)[8], Bohaty et al. (2009)[11]
TEX_{86} lowest value at MECO onset	608.84	-	40.52	This study, based on Cramwinckel et al. (2018)[8], Bohaty et al. (2009)[11]
FCO *Reticulofenestra umbilicus*	654.545	-	42.84	Shafik et al. (1998)[12], Cramwinckel et al. (2018)[8]

Supplementary Table 2: Age model for Site 1263.

Stratigraphic datum	Depth (mbsf)	Depth (adj rmcd) [Westerhold et al., 2015][13]	Age (Ma) [Pälike et al., 2006][14]	Age (Ma) [GTS 2012][5]	Source
$\delta^{13}C$ highest value	113.7	135.27	39.2	39.3	Bohaty et al. (2009)[11]
$\delta^{18}O$ final lowest value at MECO peak	119.6	141.29	39.99	40.06	Bohaty et al. (2009)[11]
$\delta^{18}O$ final highest value at MECO onset	122.6	145.83	40.552	40.52	Bohaty et al. (2009)[11]
$\delta^{13}C$ lowest value	124.9	148.13	40.925	40.81	Bohaty et al. (2009)[11]
C18r - C19n boundary	127.85	151.08	41.358	41.154	Pälike et al. (2006)[14]
C19n - C19r boundary	129.25	152.48	41.51	41.39	Pälike et al. (2006)[14]
$\delta^{13}C$ lowest value	131.6	154.8	41.796	41.64	Bohaty et al. (2009)[11]

Supplementary Table 3: Age model for Site U1333.

Stratigraphic datum	Depth (adj rmcd) [Westerhold et al., 2012][15]	Age (Ma) [Pälike et al., 2006][14]	Age (Ma) [GTS 2012][5]	Source
C17r - C18n.1n boundary	157.3	38.449	38.615	Pälike et al. (2006)[14]
T S. obtusus	158.15	38.562	38.71	Toffanin et al. (2013)[16]
T C. grandis	158.55	38.612	38.76	Toffanin et al. (2013)[16]
T C. solitus	159.95	38.788	38.92	Toffanin et al. (2013)[16]
B S. obtusus	164.15	39.314	39.4	Toffanin et al. (2013)[16]
C18n.1n - C18n.1r boundary	166.075	39.554	39.627	Pälike et al. (2006)[14]
C18n.1r - C18n.2n boundary	166.875	39.602	39.698	Pälike et al. (2006)[14]
C18n.2n - C18r boundary	169.57	40.084	40.145	Pälike et al. (2006)[14]
Bc D. hesslandii	172.69	40.421	40.41	Toffanin et al. (2013)[16]
Bc D. bisectus	172.69	40.421	40.41	Toffanin et al. (2013)[16]
T Furcatolithoides	174.5	40.614	40.56	Toffanin et al. (2013)[16]
C18r - C19n boundary	181.5	41.358	41.154	Pälike et al. (2006)[14]
C19n - C19r boundary	183.225	41.51	41.39	Pälike et al. (2006)[14]

Supplementary Table 4: Overview of all LOSCAR model scenarios. All forcings represent a gradual, linear increase/decrease to maximum values from t = 50 kyr to t = 550 kyr and are followed by a sudden drop to initial values. Initial pCO_2 concentrations were set at 750 ppmv in all simulations.

Scenario and Supplementary Figure	Silicate weathering flux	Volcanic CO_2 flux	Carbonate weathering flux
1 (5)	Feedback	+10%	Feedback
2 (5)	Feedback	+15%	Feedback
3 (5)	Feedback	+20%	Feedback
4 (6)	Constant	+10%	Constant
5 (6)	Constant	+15%	Constant
6 (6)	Constant	+20%	Constant
7 (7)	-10%	Constant	Constant
8 (7)	-15%	Constant	Constant
9 (7)	-20%	Constant	Constant
10 (8)	-5%	+5%	Constant
11 (9)	-10%	Constant	-10%
12 (10)	-10%	Constant	Feedback

Supplementary Table 5: Overview of all default Os cycle parameters. Present-day values are taken from the literature or fitted to match the present-day steady state observations. Pre-MECO values are either assumed to be similar to the present-day values or fitted to match the pre-MECO steady state observations.

Parameter	Parameter description	Value	Reference and Comments
Present-day values			
N	Os inventory in oceans	7.2×10^7 mol	Peucker-Ehrenbrink & Ravizza (2000)[17]
F_{riv}	Riverine Os flux to oceans	1800 mol/yr	Peucker-Ehrenbrink & Ravizza (2000)[17]
F_{hyd}	Hydrothermal Os flux to oceans	483 mol/yr	Calculated for steady state at R_{sw} = 1.06
F_{ext}	Extraterrestrial Os flux to oceans	80 mol/yr	Peucker-Ehrenbrink & Ravizza (2000)[17]
F_{sed}	Sedimentary Os flux from oceans	2363 mol/yr	Calculated for steady state
R_{riv}	$^{187}Os/^{188}Os$ composition of rivers	1.4	Peucker-Ehrenbrink & Ravizza (2000)[17]
R_{hyd}	$^{187}Os/^{188}Os$ composition of hydrothermal fluids	0.13	Meisel et al. (2001)[18]
R_{ext}	$^{187}Os/^{188}Os$ composition of extraterrestrial dust	0.13	Peucker-Ehrenbrink & Ravizza (2000)[17]
R_{sw}	$^{187}Os/^{188}Os$ composition of seawater	1.06	Peucker-Ehrenbrink & Ravizza (2000)[17]
Pre-MECO values			
N	Os inventory in oceans	7.2×10^7 mol	Assumed similar to present-day value
F_{riv}	Riverine Os flux to oceans	865 mol/yr	Calculated for steady state at R_{sw} = 0.55
F_{hyd}	Hydrothermal Os flux to oceans	1418 mol/yr	Calculated for steady state at R_{sw} = 0.55
F_{ext}	Extraterrestrial Os flux to oceans	80 mol/yr	Assumed similar to present-day value
F_{sed}	Sedimentary Os flux from oceans	2363 mol/yr	Assumed similar to present-day value
R_{riv}	$^{187}Os/^{188}Os$ composition of rivers	1.4	Assumed similar to present-day value
R_{hyd}	$^{187}Os/^{188}Os$ composition of hydrothermal fluids	0.13	Assumed similar to present-day value
R_{ext}	$^{187}Os/^{188}Os$ composition of extraterrestrial dust	0.13	Assumed similar to present-day value
R_{sw}	$^{187}Os/^{188}Os$ composition of seawater	0.55	This study

Supplementary References

1. Seton, M. *et al.* Global continental and ocean basin reconstructions since 200Ma. *Earth-Science Rev.* **113,** 212–270 (2012).
2. Torsvik, T. H. *et al.* Phanerozoic polar wander, palaeogeography and dynamics. *Earth-Science Rev.* **114,** 325–368 (2012).
3. Sluijs, A., Zeebe, R. E., Bijl, P. K. & Bohaty, S. M. A middle Eocene carbon cycle conundrum. *Nat. Geosci.* **6,** 429–434 (2013).
4. Cramer, B. S., Toggweiler, J. R., Wright, J. D., Katz, M. E. & Miller, K. G. Ocean overturning since the late cretaceous: Inferences from a new benthic foraminiferal isotope compilation. *Paleoceanography* **24,** 1–14 (2009).
5. Gradstein, F. M., Ogg, J. G., Schmitz, M. & Ogg, G. *The Geologic Time Scale 2012 2-Volume Set*. (Elsevier, 2012).
6. Foster, G. L., Royer, D. L. & Lunt, D. J. Future climate forcing potentially without precedent in the last 420 million years. *Nat. Commun.* **8,** 1–8 (2017).
7. Anagnostou, E. *et al.* Changing atmospheric CO_2 concentration was the primary driver of early Cenozoic climate. *Nature* **533,** 380–384 (2016).
8. Cramwinckel, M. J. *et al.* Synchronous tropical and polar temperature evolution in the Eocene. *Nature* (2018). doi:10.1038/s41586-018-0272-2
9. Gradstein, F. M., Ogg, J. G. & Smith, A. G. *A Geologic Time Scale 2004*. (Cambridge University Press, 2005).
10. Ravizza, G. E. & Paquay, F. S. Os isotope chemostratigraphy applied to organic-rich marine sediments from the Eocene-Oligocene transition on the West African margin (ODP Site 959). *Paleoceanography* **23,** (2008).
11. Bohaty, S. M., Zachos, J. C., Florindo, F. & Delaney, M. L. Coupled greenhouse warming and deep-sea acidification in the middle Eocene. *Paleoceanography* **24,** (2009).
12. Shafik, S., Watkins, D. K. & Shin, I. C. Calcareous Nannofossil Paleogene Biostratigraphy, Côte D'Ivoire-Ghana Marginal Ridge, Eastern Equatorial Atlantic. *Proc. Ocean Drill. Program, Sci. Results* **159,** 413–431 (1998).
13. Westerhold, T., Röhl, U., Frederichs, T., Bohaty, S. M. & Zachos, J. C. Astronomical calibration of the geological timescale: Closing the middle Eocene gap. *Clim. Past* **11,** 1181–1195 (2015).
14. Pälike, H. *et al.* The heartbeat of the Oligocene climate system. *Science* **314,** 1894–

1898 (2006).

15. Westerhold, T. *et al.* Revised composite depth scales and integration of IODP Sites U1331-U1334 and ODP Sites 1218-1220. *Proc. Integr. Ocean Drill. Progr.* **320,** (2012).
16. Toffanin, F., Agnini, C., Rio, D., Acton, G. & Westerhold, T. Middle Eocene to early Oligocene calcareous nannofossil biostratigraphy at IODP Site U1333 (equatorial Pacific). *Micropaleontology* **59,** 69–82 (2013).
17. Peucker-Ehrenbrink, B. & Ravizza, G. E. The marine osmium isotope record. *Terra Nov.* **12,** 205–219 (2000).
18. Meisel, T., Walker, R. J., Irving, A. J. & Lorand, J. P. Osmium isotopic compositions of mantle xenoliths: A global perspective. *Geochim. Cosmochim. Acta* **65,** 1311–1323 (2001).